Journal of Atmospheric and Solar-Terrestrial Physics 71 (2009) 531–551

Contents lists available at ScienceDirect

Journal of
Atmospheric and Solar-Terrestrial Physics

journal homepage: www.elsevier.com/locate/jastp

High-altitude data assimilation system experiments for the northern summer mesosphere season of 2007

Stephen D. Eckermann [a,*], Karl W. Hoppel [b], Lawrence Coy [a], John P. McCormack [a], David E. Siskind [a], Kim Nielsen [c], Andrew Kochenash [c], Michael H. Stevens [a], Christoph R. Englert [a], Werner Singer [d], Mark Hervig [e]

[a] Space Science Division, Naval Research Laboratory, Washington, DC, USA
[b] Remote Sensing Division, Naval Research Laboratory, Washington, DC, USA
[c] Computational Physics, Inc., Springfield, VA, USA
[d] Leibniz Institute of Atmospheric Physics, Kühlungsborn, Germany
[e] GATS, Inc., Driggs, ID, USA

ARTICLE INFO

Article history:
Accepted 28 September 2008
Available online 1 November 2008

Keywords:
Data assimilation
Polar mesospheric cloud
Tide
Planetary wave
Mesosphere

ABSTRACT

A global numerical weather prediction system is extended to the mesosphere and lower thermosphere (MLT) and used to assimilate high-altitude satellite measurements of temperature, water vapor and ozone from MLS and SABER during May–July 2007. Assimilated temperature and humidity from 100 to 0.001 hPa show minimal biases compared to satellite data and existing analysis fields. Saturation ratios derived diagnostically from these assimilated temperature and water vapor fields at PMC altitudes and latitudes compare well with seasonal variations in PMC frequency measured from the aeronomy of ice in the mesosphere (AIM) satellite. Synoptic maps of these diagnostic saturation ratios correlate geographically with three independent transient mesospheric cloud events observed at midlatitudes by SHIMMER on STPSat-1 and by ground observers during June 2007. Assimilated temperatures and winds reveal broadly realistic amplitudes of the quasi 5-day wave and migrating tides as a function of latitude and height. For example, analyzed winds capture the dominant semidiurnal MLT wind patterns at 55°N in June 2007 measured independently by a meteor radar. The 5-day wave and migrating diurnal tide also modulate water vapor mixing ratios in the polar summer MLT. Possible origins of this variability are discussed.

Published by Elsevier Ltd.

1. Introduction

Global numerical weather prediction (NWP) systems consist of two main components: a forecast model that predicts future atmospheric conditions, and a data assimilation system (DAS) that provides global initial conditions for those forecasts based on available observations. The quality of the DAS products, and hence the skill of the resulting forecasts, rely heavily on the high-density planetary-scale measurements provided from satellites.

The maturity and sophistication of NWP DASs have now led them to assimilate satellite radiances directly, since the forecast models now provide more accurate a priori estimates than the climatologies typically used in standard satellite retrievals. Radiance weighting functions, however, are typically vertically broad, with some having long "tails" that extend to high altitudes not covered by the forecast model component. This latter restriction reduces the accuracy of the radiance assimilation, and can prevent certain channels from being assimilated. Thus most operational centers are progressively increasing the vertical range of their NWP systems to span most of the stratosphere, with a few now extending into the lower mesosphere.

Currently, however, no operational NWP system extends through the mesosphere and lower thermosphere (MLT), due primarily to a lack of operational radiance channels in this altitude range. This is changing with the launch of the latest generation of operational sensors, such as the special sensor microwave imager/sounder (SSMIS) (Lipton, 2002; Kerola, 2006), and the advent of fast radiative transfer codes suitable for assimilating MLT radiances operationally (Han et al., 2007). Thus research NWP systems extending into the MLT are now being actively developed (Polavarapu et al., 2005a; Hoppel et al., 2008). Since the boundary between atmosphere and space is defined arbitrarily at an MLT altitude of either 80 or 100 km, such systems represent the first steps towards a truly integrated global ground-to-space forecasting capability. Here we work with one such developmental ground-to-MLT NWP system: the advanced level

* Corresponding author. Tel.: +1 202 404 1299; fax: +1 202 404 8090.
E-mail address: stephen.eckermann@nrl.navy.mil (S.D. Eckermann).

1364-6826/$ - see front matter Published by Elsevier Ltd.
doi:10.1016/j.jastp.2008.09.036

Report Documentation Page

Form Approved
OMB No. 0704-0188

1. REPORT DATE	2. REPORT TYPE	3. DATES COVERED
SEP 2008		**00-00-2008 to 00-00-2008**

4. TITLE AND SUBTITLE	5a. CONTRACT NUMBER
High-altitude data assimilation system experiments for the northern summer mesosphere season of 2007	5b. GRANT NUMBER
	5c. PROGRAM ELEMENT NUMBER
6. AUTHOR(S)	5d. PROJECT NUMBER
	5e. TASK NUMBER
	5f. WORK UNIT NUMBER
7. PERFORMING ORGANIZATION NAME(S) AND ADDRESS(ES) **Naval Research Laboratory,Space Science Division,Washington,DC,20375**	8. PERFORMING ORGANIZATION REPORT NUMBER
9. SPONSORING/MONITORING AGENCY NAME(S) AND ADDRESS(ES)	10. SPONSOR/MONITOR'S ACRONYM(S)
	11. SPONSOR/MONITOR'S REPORT NUMBER(S)

12. DISTRIBUTION/AVAILABILITY STATEMENT
Approved for public release; distribution unlimited

13. SUPPLEMENTARY NOTES

14. ABSTRACT

A global numerical weather prediction system is extended to the mesosphere and lower thermosphere MLT)and used to assimilate high-altitude satellite measurements of temperature, water vapor and ozone from MLS and SABER during May-July 2007. Assimilated temperature and humidity from 100 to 0.001 hPa show minimal biases compared to satellite data and existing analysis fields. Saturation ratiosderived diagnostically from these assimilated temperature and water vapor fields at PMC altitudes and latitudes compare well with seasonal variations in PM Cfrequency measured from the aeronomy of ice in themesosphere (AIM)satellite. Synoptic maps of these diagnostic saturation ratios correlate geographically with three independent transient mesospheric cloud events observed at midlatitudes by SHIMMER on STPSat-1 and by ground observers during June 2007. Assimilated temperatures and winds reveal broadly realistic amplitudes of the quasi 5-day wave and migrating tides as a function of latitude and height. For example, analyzed winds capture the dominant semidiurnal MLT wind patterns at 551N in June 2007 measured independently by a meteor radar. The 5-day wave and migrating diurnal tide also modulate water vapor mixing ratios in the polar summer MLT. Possible origins of this variability are discussed.

15. SUBJECT TERMS

16. SECURITY CLASSIFICATION OF:			17. LIMITATION OF ABSTRACT	18. NUMBER OF PAGES	19a. NAME OF RESPONSIBLE PERSON
a. REPORT **unclassified**	b. ABSTRACT **unclassified**	c. THIS PAGE **unclassified**	**Same as Report (SAR)**	**21**	

physics high-altitude (ALPHA) prototype of the navy operational global atmospheric prediction system (NOGAPS), which we describe in Section 2.

Adding an MLT component to an NWP system presents a variety of technical challenges that are only just beginning to be grappled with. The vertically extended forecast model must include new physical processes appropriate for the MLT. Coupling the forecast model to the DAS raises further issues, such as vertical information transfer, model-data biases, appropriate dynamical balance constraints, and resolved and parameterized gravity wave dynamics (Polavarapu et al., 2005b; Sankey et al., 2007). In developing and testing new MLT components, research MLT data, such as provided by the aeronomy of ice in the mesosphere (AIM) satellite (Russell et al., 2008), are particularly valuable, either for direct assimilation into the system or for independent validation of MLT DAS output.

Research satellites typically measure only a targeted subset of atmospheric parameters specific to their core science objectives, usually within a limited range of longitudes, latitudes, heights and local times. AIM, for example, consists of the solar occultation for ice experiment (SOFIE), which performs limb occultation measurements of temperature and constituents within a narrow band of latitudes at a fixed local time (Gordley et al., 2008), and the cloud imaging and particle size (CIPS) instrument, which images polar mesospheric cloud (PMC) properties in the nadir (McLintock et al., 2008). By contrast, NWP systems can assimilate data from a range of satellite and suborbital instruments to provide an optimal global state estimate, filling any spatial or temporal gaps using the global model's full-physics forecast fields constrained by DAS-based initial conditions. The synoptic gridded analysis products that result are more amenable to research studies, while providing a range of other atmospheric parameters that may not be measured directly (e.g., winds). The scientific value of such DAS products for NASA's middle atmosphere satellite research missions is already well established. Global analysis fields generated by the Met Office DAS, for instance, provided pivotal independent meteorological support for upper atmosphere research satellite (UARS) observations and science (Lahoz and O'Neill, 1998), while NASA's Global Modeling and Assimilation Office (GMAO) GEOS DAS analyses play a similar central support role in the current Aura and Aqua missions (Susskind et al., 2006; Manney et al., 2007). Thus one motivation for the present work is to generate synoptic analysis fields extending into the MLT that provide analogous support for AIM.

There are many ways in which ground-to-MLT DAS fields could contribute to the science return from AIM. For example, there is debate as to the role of vertical and latitudinal tidal and planetary wave transport in controlling PMC variability (e.g., Berger and von Zahn, 2007; Gerding et al., 2007; Stevens et al., 2008). The limited local time coverage of satellite MLT measurements, however, presents well-known difficulties in isolating mean, tidal and fast planetary wave signatures. Data analysis studies to date have employed complex asynoptic mapping or least-squares fitting algorithms that require assumptions about stationarity, aliasing and seasonal dependences (e.g., Wu et al., 1995; Burrage et al., 1995; Forbes et al., 1997; Zhu et al., 2005). While these assumptions can be tested and the procedures improved with the help of MLT fields from general circulation models (GCMs) (Oberheide et al., 2003; McLandress and Zhang, 2007) and addition of data from other instruments (Drob et al., 2000; Azeem et al., 2000), final mean mesospheric temperature estimates from these algorithms can still have large uncertainties (Drob et al., 2000; Oberheide et al., 2003; Zhu et al., 2005). NWP systems combine aspects of all the aforementioned algorithms by optimally assimilating MLT data from a variety of sources with the aid of a full-physics GCM to constrain the system dynamically and optimally fill gaps. The physical and dynamical constraints of the system yield additional benefits, such as estimates of atmospheric parameters not directly measured, such as winds. Furthermore, mean and root-mean-square (RMS) differences between the model forecasts (F), observations (O) and the analysis fields (A) provide objective quantification of the inherent biases and uncertainties of all the analyzed physical quantities output by the system.

We explore these potential benefits for MLT science in this paper. After describing the system (forecast model, DAS and satellite observations) in Section 2 and tuning it in Section 3, we validate its output against independent observations and analysis fields in Section 4. In Section 5 we study the seasonal variation of assimilated temperature and water vapor fields at PMC altitudes and compare with corresponding independent PMC observations from AIM. Section 6 studies planetary wave signals in the analysis fields, focusing on the quasi 5-day wave and solar migrating tides near PMC regions. Section 7 applies the synoptic analysis fields to midlatitude mesospheric cloud (MC) events reported at specific geographical locations in June 2007. Section 8 summarizes the major findings of these assimilation experiments and assesses near-term development needs for the system to improve MLT products in future assimilation experiments.

2. NOGAPS-ALPHA

Here we briefly describe the salient aspects of the NOGAPS-ALPHA system used in this study. Hoppel et al. (2008) provide a complete overview of the initial system developed for data assimilation research.

2.1. Forecast model component

Hogan and Rosmond (1991) and Hogan et al. (1991) provide detailed descriptions of the NOGAPS global forecast model. Briefly, the dynamical core is Eulerian, hydrostatic, spectral in the horizontal and finite difference in the vertical, using the Lorenz-grid vertical discretization of Arakawa and Suarez (1983) generalized to hybrid vertical coordinates following Simmons and Burridge (1981). The model uses a three-time-level scheme incorporating a semi-implicit treatment of gravity wave propagation, implicit zonal advection of moisture and constituents, and Robert (Asselin) time filtering. The operational model's physical parameterizations include vertical diffusive transport in the planetary boundary layer (Louis, 1979; Louis et al., 1982) coupled to a land surface model (Hogan, 2007), orographic gravity-wave and flow-blocking drag (Webster et al., 2003), shallow cumulus mixing (Tiedtke, 1984), deep cumulus convection (Peng et al., 2004), convective, stratiform and boundary layer clouds and precipitation (Slingo, 1987; Teixeira and Hogan, 2002), and shortwave and longwave radiation (Harshvardhan et al., 1987). At the Fleet Numerical Meteorological and Oceanographic Center (FNMOC) NOGAPS runs operationally at T239L30 (T119L30 for ensemble forecasts) using mean orography, pure σ levels, and a rigid upper boundary at $p_{top} = 1$ hPa.

The progressive extension of this forecast model through the stratosphere and into the lower mesosphere for NOGAPS-ALPHA has been described, for example, by Eckermann et al. (2004) and Allen et al. (2006). We briefly summarize salient additions here, focusing mostly on new physical parameterizations required to forecast the MLT and support the DAS at these altitudes. One important point to note is that the aforementioned NOGAPS cloud physics schemes have not been extended into the middle atmosphere to model either stratospheric clouds or MCs.

2.1.1. Resolution and height range

As in Hoppel et al. (2008) the forecast model is run here at a triangular spectral truncation of T79, corresponding to 1.5° latitude–longitude resolution on the quadratic Gaussian grid. We use 68 model layers that extend into the MLT ($p_{top} = 5 \times 10^{-4}$ hPa) with a vertical pressure height resolution $\Delta Z \approx 2$ km throughout the middle atmosphere. The runs here use the "NEWHYB2" hybrid vertical coordinate described by Eckermann (2008) with $k_p = 43$ isobaric model layers between p_{top} and $p_{k_p+1/2} \sim 87.4$ hPa. This new hybrid coordinate reduces vertical truncation errors in the stratosphere and MLT (Eckermann, 2008) and should improve the quality of the assimilations above the tropopause (see, e.g., Trenberth and Stepaniak, 2002).

2.1.2. Radiation

The high-altitude forecast model has been designed to switch easily between any of the operational or research physics packages. Thus, while the operational Harshvardhan et al. (1987) radiation schemes can be used, NOGAPS-ALPHA runs here use different schemes that extend to MLT altitudes. Radiative heating rates are computed using the Chou and Suarez (1999) scheme. We deactivate that scheme's near-infrared (IR) CO_2 band contribution, following Eckermann et al. (2007), since it lacks any non-local thermodynamic equilibrium (non-LTE) modifications and thus substantially overestimates high-altitude near-IR heating rates (Fomichev et al., 2004). Longwave cooling rates are computed using the parameterization of Chou et al. (2001), which is accurate from the ground to 0.01 hPa, and of Fomichev et al. (1998), which includes non-LTE effects on IR CO_2 emissions at MLT altitudes. The two profiles $Q_{Chou}(Z)$ and $Q_{Fomichev}(Z)$ are blended into a final cooling rate profile

$$Q(Z) = w(Z)Q_{Chou}(Z) + [1 - w\,(Z)]Q_{Fomichev}(Z), \tag{1}$$

using a pressure-height dependent linear weight

$$w(Z) = \frac{1 - \tanh\left(\dfrac{Z - Z_{int}}{\zeta}\right)}{2}, \tag{2}$$

where $Z_{int} = 75$ km and $\zeta = 5$ km. Due to the computational expense, here we update radiative heating and cooling rates every 2 h.

2.1.3. Trace constituents

Specific humidity q is built into the discretized NOGAPS primitive equations through the virtual potential temperature. Thus NOGAPS-ALPHA must initialize and forecast it accurately from the surface to the MLT. In addition to NOGAPS tropospheric moist physics parameterizations, we model water vapor production in the stratosphere due to methane oxidation and photolytic loss in the mesosphere using the parameterization of McCormack et al. (2008). The latter yields photochemical lifetimes of a few days near the polar summer mesopause (see Table 6 of McCormack et al., 2008) and thus can influence 6-hourly water vapor forecasts and assimilations at PMC altitudes. Only prognostic q values below 200 hPa altitude are used in the radiation calculations: above, values from observational and model-based climatologies are used (see Section 3.1.1.1 of Eckermann et al., 2007, for details).

The forecast model incorporates a prognostic capability for ozone, with a number of ozone photochemistry parameterizations available for use (Eckermann et al., 2004; McCormack et al., 2004). Here we use the scheme of McCormack et al. (2006) that runs operationally in the National Centers for Environmental Prediction Global Forecast System (NCEP GFS). It uses lookup tables of diurnally averaged photochemical coefficients derived from a full chemistry model based on linearizing scaled odd-oxygen production and loss rates about equilibrium states. These equilibrium states are specified in the model using zonal-mean observational climatologies that are chosen carefully here to match characteristics of the assimilated ozone observations so as to avoid model-data bias (Geer et al., 2007; Coy et al., 2007). The scheme does not at present parameterize either diurnal ozone photochemistry at altitudes above ~0.3 hPa or tropospheric ozone chemistry, relaxing ozone in both altitude regions to a reference state based on a mean photochemical relaxation rate. Because of this, here we do not use prognostic ozone mixing ratios χ_{O3} in the radiation calculations. Instead we use the observational ozone climatology described by Eckermann et al. (2007) that incorporates daytime ozone data only at high altitudes. That climatology was improved slightly here by adding high-altitude daytime ozone data from the High Resolution Doppler Imager (Marsh et al., 2002) at the very highest altitudes. These daytime ozone climatologies improve the model's radiative heating rates (Eckermann et al., 2007) which are important for accurately modeling and assimilating temperature at these altitudes (e.g., Sassi et al., 2005). For simplicity, the night-to-day ratio used by Eckermann et al. (2007) to scale up nighttime ozone values for the cooling rate calculations was not used since it is a more minor effect for temperature prediction.

2.1.4. Gravity wave drag

Nonorographic gravity wave drag (GWD) is the most important new parameterization required for summer MLT prediction (e.g., Fritts and Luo, 1995). Here we use a multiwave scheme based on the linear GW saturation formulation of Lindzen (1981), as developed for the whole atmosphere community climate model (WACCM). Appendix A of Garcia et al. (2007) provides a detailed description. Here we summarize the important aspects for the present work.

The scheme launches a prescribed spectrum of n_{gw} individual GWs within every grid box at a source level set here to 500 hPa (following Garcia et al., 2007). Each GW j is assigned a unique ground-based horizontal phase speed

$$c_j = |U_{500}| + j\Delta c,$$
$$j = -n_c, -n_c + 1, \ldots + n_c - 1, +n_c \quad (j \in \mathbf{Z}, n_c \in \mathbf{N}), \tag{3}$$

such that phase speeds are distributed symmetrically with respect to the 500 hPa horizontal wind speed $|U_{500}|$. As in Garcia et al. (2007) we choose $\Delta c = 2.5\,\mathrm{m\,s^{-1}}$ and $n_c = 32$, yielding $n_{gw} = 2n_c + 1 = 65$ component gravity waves with intrinsic phase speeds $|c_j - U_{500}|$ distributed between $\pm 80\,\mathrm{m\,s^{-1}}$, all aligned along the 500 hPa wind speed direction. The vertical flux of horizontal pseudomomentum density (Eliassen-Palm flux) of each wave, $\tau_{src}(c_j)$, is assigned based on a Gaussian flux distribution versus phase speed, centered about $|U_{500}|$, of the form

$$\tau_{src}(c_j) = \tau_b F(\phi, t) \exp\left[\frac{-(c_j - c_{j=0})^2}{\hat{c}_w^2}\right]. \tag{4}$$

Following Garcia et al. (2007) we set the phase-speed width $\hat{c}_w = 30\,\mathrm{m\,s^{-1}}$ and tune the so-called background flux τ_b in experiments described in Section 3. The function $F(\phi, t)$, plotted in Fig. 1, is an analytical fit as a function of latitude ϕ and time (month) t to results obtained from diagnostically processing long-term climate model output using a proposed parameterization of frontogenetic gravity wave generation (cf. Fig. 2 of Charron and Manzini, 2002). It yields a large winter–summer flux asymmetry in each hemisphere as well as a gradual variation during the season: see Garcia et al. (2007) for further details.

Wave propagation, wave breaking and saturation, and resulting diffusive and thermal dissipation of wave momentum flux are

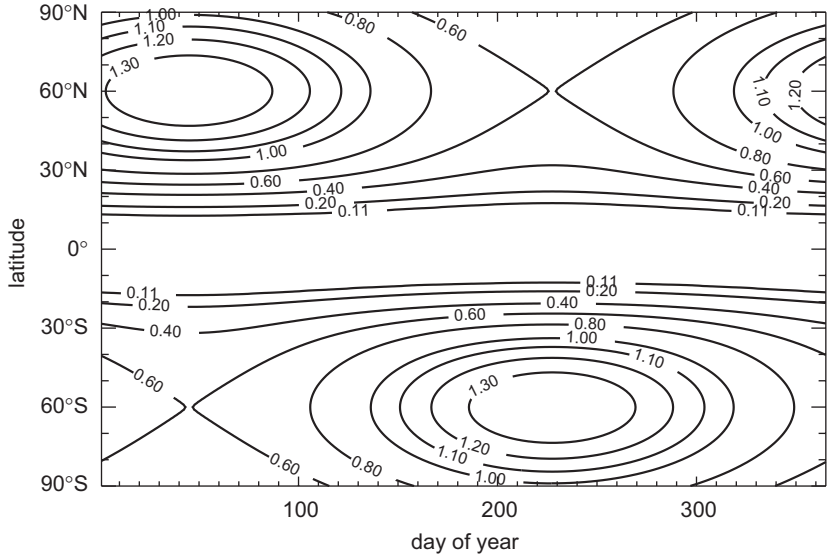

Fig. 1. Nonorographic GWD source function $F(\phi, t)$.

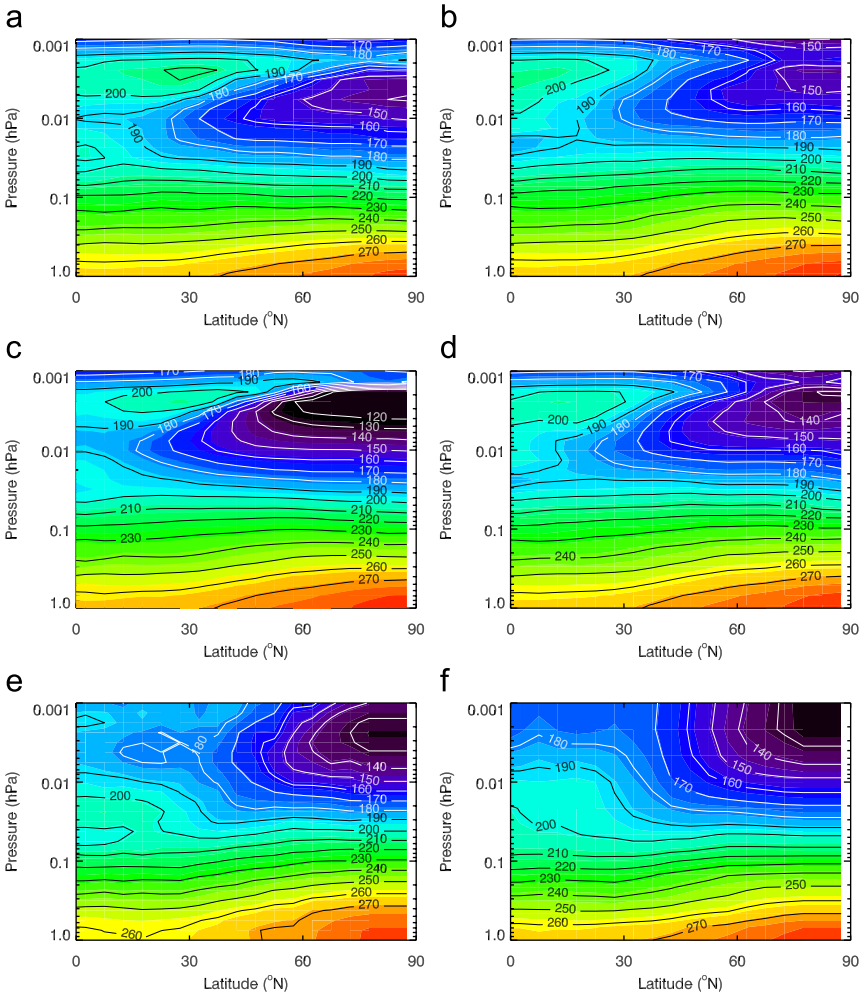

Fig. 2. Zonal-mean northern-hemisphere temperatures from 1 to 0.001 hPa of four NOGAPS-ALPHA +14 day forecasts, initialized on 1 June 2007 using preliminary high-altitude analysis fields and the following nonorographic GWD parameter settings: (a) $\tau_b = 7$ mPa, $\varepsilon = 0.0125$; (b) $\tau_b = 1.75$ mPa, $\varepsilon = 0.0125$; (c) $\tau_b = 1.75$ mPa, $\varepsilon = 0.0250$; (d) $\tau_b = 1.75$ mPa, $\varepsilon = 0.0175$. Panels (e) and (f) show zonal-mean SABER and MLS temperatures, respectively, on 15 June. Temperatures below 120 K are not contoured.

modeled for each wave as in Garcia et al. (2007). At model layer k, the ensuing GW-induced mean-flow acceleration due to wave j is

$$a_{j,k} = -g\varepsilon\frac{\partial\tau_{j,k}}{\partial p}, \tag{5}$$

where g is gravitational acceleration and p is pressure. This acceleration, directed along the 500 hPa (source-level) wind speed direction, is apportioned to modify zonal and meridional wind speeds accordingly, and summed over all GWs j. All remaining flux is deposited in the top two model layers to conserve momentum so as to capture robust downward-control responses (Shaw and Shepherd, 2007).

The factor ε in (5) is a constant set in the range $0 \leqslant \varepsilon \leqslant 1$. Such normalization terms occur routinely in Lindzen-type schemes to ameliorate excessively large and/or insufficiently smooth GWD in models, and are usually justified physically as encapsulating either the net "efficiency" of wave breaking or the net "intermittency" of GW activity, either in time (due to variable forcing) or spatially due to incomplete filling of the grid box by the GW packets. The mathematical implementation of the efficiency concept in (5), which follows that used in the Alexander and Dunkerton (1999) scheme, simply scales down all the GWD values by a constant amount. It should be noted that similar efficiency factors are implemented in different ways mathematically in other Lindzen schemes, where they act differently and modify both the shape and magnitude of the GWD profile (Hamilton, 1997; McLandress, 1998; Norton and Thuburn, 1999). The specific implementation here has the practical advantage that source flux parameters like τ_b can be adjusted to modify the shape of the GWD profile, whereupon ε can then be adjusted to scale the final GWD while retaining the tuned profile shape. Specific GWD tuning for the NOGAPS-ALPHA assimilation runs is discussed in Section 3.

For the experiments reported here, we apply only the scheme's GW momentum flux divergence tendencies to the model: GWD-induced vertical diffusivities, while calculated, are not at present used to mix momentum, heat or constituents in the model. Orographic GWD is applied separately using either a Palmer et al. (1986) or Webster et al. (2003) scheme: we choose the former here following Siskind et al. (2007).

2.2. DAS component

The NOGAPS-ALPHA DAS uses a three-dimensional variational (3DVAR) algorithm formulated in observational space, known as the Naval Research Laboratory (NRL) Atmospheric Variational DAS, or NAVDAS. The basic formulation and initial performance are described by Daley and Barker (2001a), while Daley and Barker (2001b) provide a more detailed description. Hoppel et al. (2008) explain how NAVDAS was interfaced to the NOGAPS-ALPHA forecast model to run as an NWP system extending into the MLT. The version and setup used here are very similar to those described by Hoppel et al. (2008), and so we focus here mainly on an overview of that system and salient differences for the experiments reported here.

Given a column vector $\mathbf{x_b}$ containing I "background" estimates of some atmospheric parameter (e.g., temperature) and L estimates of some related observation $\mathbf{y}$ (e.g., thermal radiance), NAVDAS generates a corresponding analysis vector $\mathbf{x_a}$ by numerically minimizing the scalar cost function

$$J(\mathbf{x_a}) = (\mathbf{y} - \mathscr{H}(\mathbf{x_a}))^{\mathrm{T}}\mathbf{R}^{-1}(\mathbf{y} - \mathscr{H}(\mathbf{x_a})) + (\mathbf{x_b} - \mathbf{x_a})^{\mathrm{T}}\mathbf{P_b}^{-1}(\mathbf{x_b} - \mathbf{x_a}). \tag{6}$$

Here $\mathscr{H}$ is the forward observation operator (e.g., a radiative transfer forward model that converts temperature into radiance) and $\mathbf{R}$ is the $L \times L$ error covariance matrix of the observations: similarly $\mathbf{P_b}$ is the $I \times I$ error covariance matrix of the background, and T denotes transpose. Eq. (6) is identical in form to cost functions solved in standard satellite retrievals except here the background $\mathbf{x_b}$ is provided by the forecast model.

The observation-space solution to (6) is (Daley and Barker, 2001a)

$$\mathbf{x_a} - \mathbf{x_b} = \mathbf{P_b}\mathbf{H}^{\mathrm{T}}[\mathbf{H}\mathbf{P_b}\mathbf{H}^{\mathrm{T}} + \mathbf{R}][\mathbf{y} - \mathscr{H}(\mathbf{x_b})], \tag{7}$$

which converts the so-called innovations $\mathbf{y} - \mathscr{H}(\mathbf{x_b})$ in the observation space into a correction vector $\mathbf{x_a} - \mathbf{x_b}$ in model/analysis space. The matrix $\mathbf{H} = \partial\mathscr{H}/\partial\mathbf{x}|_{\mathbf{x_b}}$ originates as an approximation of $\mathscr{H}(\mathbf{x_a})$ by the truncated Taylor series expansion $\mathscr{H}(\mathbf{x_b}) + \mathbf{H}[\mathbf{x_a} - \mathbf{x_b}]$. The accuracy of this approximation, and hence the quality of the analysis, clearly requires *inter alia* that $\mathbf{x_a} - \mathbf{x_b}$ be as small as possible, and thus that the forecast model be minimally biased with respect to both observations and analysis (see Section 3). Here we use a standard 6-h update cycle, so that $\mathbf{x_b}$ in (7) is the 6-h forecast from the previous cycle. We compute the observation-space innovations $\mathbf{y} - \mathscr{H}(\mathbf{x_b})$ in (7) by interpolating the 3, 6 and 9 h forecasts $\mathbf{x_b}$ from the previous cycle to the times and locations of the observation vector $\mathbf{y}$, forward modeling where necessary. This corresponds to a low time-resolution 3DVAR-FGAT (first guess at appropriate time) algorithm (Lorenc and Rawlins, 2005).

Our research forecast-assimilation runs with NOGAPS-ALPHA use the archived sensor data routinely assimilated operationally by NOGAPS at FNMOC (see Table 1 of Baker et al., 2007). Most relevant here for the middle atmosphere are advanced microwave sounding unit (AMSU-A) thermal radiances from stratospheric channels 9 and 10 on the NOAA-15 and NOAA-16 satellites. We use the NAVDAS operational data-thinning schemes for these radiances described by Baker et al. (2005).

In the initial NOGAPS-ALPHA implementation, Hoppel et al. (2008) assimilated limb-scanned temperature data from:

- the microwave limb sounder (MLS) on the Aura satellite from 32-0.01 hPa (version 2.2 retrievals: see Schwartz et al., 2008);
- the sounding of the atmosphere using broadband emission radiometry (SABER) instrument on the thermosphere ionosphere mesosphere energetics and dynamics (TIMED) satellite from 32-0.019 hPa (version 1.06 retrievals: see Mertens et al., 2004).

In this study we also assimilate SABER and MLS temperatures using the same observation operators and error covariances for these instruments described by Hoppel et al. (2008). Here, however, we use version 1.07 SABER retrievals (Remsberg et al., 2008) that account for vibrational exchange between CO_2 isotopes, which Kutepov et al. (2006) have shown is critical to retrieving accurate temperatures in the summer mesopause (Garcia-Comas et al., 2008).

Here we assimilate SABER and MLS temperatures up to a higher altitude of 0.002 hPa, in order to insert data at polar summer mesopause altitudes. As in Hoppel et al. (2008) the increments above this top data insertion level are progressively damped over a ~6 km pressure height range, before reverting thereafter to pure forecast fields. Hoppel et al. (2008) fitted and removed a global mean vertical profile of the bias between MLS and SABER temperatures, using it to bias-correct the SABER data and keeping MLS temperatures unchanged. Here we compute a similar profile over the May–June 2007 period using version 1.07 SABER data, but use it to bias-correct SABER temperatures only at altitudes below 2.7 hPa, where SABER has a 1–3 K warm bias

relative to MLS and other instruments (Schwartz et al., 2008; Remsberg et al., 2008). At higher altitudes, V1.07 SABER temperatures appear to be accurate to within ~1−2 K (Remsberg et al., 2008) whereas V2.2 MLS temperatures have a vertically structured bias near the stratopause and a systematic cold bias throughout the mesosphere (Schwartz et al., 2008). Thus, at altitudes above ~2 hPa we bias-correct MLS temperatures using a profile based on a subjective fit to the various profiles of mean bias of MLS relative to other satellite, suborbital and analysis temperatures plotted in Fig. 26 of Schwartz et al. (2008). Background error covariances are specified statically as in Hoppel et al. (2008).

PMC formation and microphysics depend on not just temperature but water vapor abundances, which in turn depend on HO_x/O_x chemistry. Thus in these experiments we also assimilate version 2.2 MLS retrievals of water vapor mixing ratios, χ_{H_2O}, and ozone mixing ratios, χ_{O_3}.

Lambert et al. (2007) and Read et al. (2007) provide detailed descriptions and validation of the version 2.2 MLS χ_{H_2O} retrievals at upper and lower altitudes, respectively. They recommend that science studies using these data be confined to the 316–0.002 hPa range. Here we assimilate MLS χ_{H_2O} profiles from 220 to 0.002 hPa. While the precision of individual χ_{H_2O} estimates is ~4−8% throughout the stratosphere and lower mesosphere, it degrades with increasing height in the mesosphere to ~18% at 0.02 hPa and ~180% at 0.002 hPa (see Table 2 of Lambert et al., 2007). To reduce upper-level measurement uncertainties prior to assimilation, for $p \leqslant 0.02$ hPa we apply a three-point along-track running average to the raw χ_{H_2O} profiles and repeat the process for $p \leqslant 0.005$ hPa. We use horizontal correlation lengths of 358 km for these data, consistent with mean horizontal resolution in Table 2 of Lambert et al. (2007). The intrinsic vertical resolution of these data increases with altitude but, as for MLS temperatures, we use constant vertical Gaussian averaging with a full-width half-maximum (FWHM) of ~2 km: see Section 3.2 of Hoppel et al. (2008) for additional discussion.

We assimilate MLS χ_{O_3} profiles from 215 to 0.02 hPa, the same validated range quoted in Table 1 of Jiang et al. (2007), who showed good agreement with suborbital ozone profiles throughout the middle atmosphere. Since the forecast model does not parameterize diurnal ozone photochemistry (see Section 2.1), we assimilate only daytime values at altitudes above 1 hPa. The vertical resolution of the data is ~3 km throughout the range, which we use as our vertical averaging FWHM for these data in the DAS along with the same horizontal correlation lengths of ~380 km used for MLS temperature.

The system runs in a standard 6-h forecast-assimilation cycle, which presents challenges for assimilating tides (Swinbank et al., 1999): given their importance in the MLT, the following choices were made to aid assimilation of tidal features. Nonlinear normal-mode initialization (NNMI) of the analysis state by the forecast model was deactivated, given that it mishandles migrating tides (Wergen, 1989). NOGAPS-ALPHA can perform NNMI on the analysis increments only, which treats tides at lower altitudes much better while still eliminating gravity wave noise (Ballish et al., 1992; Seaman et al., 1995). However, since its potential impact at new MLT altitudes has not been methodically investigated, we opted to deactivate it too and thus performed no initial-state filtering of the analysis prior to running forecasts. Work by Sankey et al. (2007) with the Canadian middle atmosphere model (CMAM) suggests that the additional resulting GW noise in the forecast can propagate into the MLT and break, affecting mean and tidal structures, with some damping of tidal amplitude and spreading of tidal frequencies: nonetheless, their work indicates that broadly realistic diurnal and semidiurnal tides are still captured in the MLT fields.

3. Reduction of model bias by tuning the GWD parameterization

Biases in model forecasts yield biased analysis fields (Dee and daSilva, 1998). Thus, prior to commencing the assimilation runs reported here, we performed an iterative series of 2-week forecasts that were initialized to high-altitudes at various times in June 2007 using output from a one-month test assimilation. The forecasts of zonal-mean temperature were compared with time series of MLS and SABER zonal-mean temperatures at various latitudes and pressures. These comparisons led to adjustment of the background flux τ_b and/or efficiency ε used in the nonorographic GWD scheme (see Section 2.1.4), whereupon the forecasts and comparisons were repeated until the forecast temperatures were close to the observations throughout June, focusing especially on the polar summer MLT.

The top four panels in Fig. 2 summarize results of four different forecast experiments each initialized on 1 June, showing zonal-mean summer hemisphere temperatures after +14 days. Forecasts in Fig. 2a used the default τ_b and ε settings of Hoppel et al. (2008) and yield a polar summer mesopause that is located too low in altitude, followed by an unrealistically sharp temperature gradient yielding a thin warm layer at ~0.002 hPa: zonal-mean SABER and MLS temperatures on 15 June 2007 are shown for reference in Figs. 2e and f, respectively. Reducing τ_b by a factor of 4 to 1.75 mPa yields forecast temperatures in Fig. 2b that all but eliminate the secondary warm layer and generate a polar summer mesopause at roughly the right altitude, but which is too warm relative to MLS and SABER. Increasing ε by a factor of 2 yields an excessively cold mesopause (Fig. 2c). An intermediate choice of $\varepsilon = 0.0175$ yields zonal-mean forecast temperatures in Fig. 2d with a polar summer mesopause of about the right altitude and temperature according to both SABER and MLS. Forecasts initialized at other times in June (not shown) produce similarly good results using these settings.

Changes in τ_b and ε above apply globally to reduce GWD in the winter (southern) hemisphere as well, where they yield forecast temperatures that compare less favorably with MLS and SABER due to reduced diabatic descent. Thus we performed additional forecasts that retained the tuned summer GWD settings in Fig. 2d but increased winter GWD by scaling up $F(\phi, t)$ in the south (see Fig. 1). A series of these experiments (not shown) yielded summer MLT forecasts consistently poorer than Fig. 2d, due to the indirect effects of increased winter GWD on summer MLT temperatures through a modified mesospheric residual circulation (Becker and Fritts, 2006). Thus we settled here upon tuned GWD settings of $\tau_b = 1.75$ mPa and $\varepsilon = 0.0175$ for our final assimilation run to reduce the potential for large mean O-F (innovation) biases in the summer MLT, with the understanding that forecast biases may arise in the winter hemisphere.

4. Initial validation

Our assimilation run extends over nearly a full PMC season, from 15 May 2007 to 31 August 2007. However, on 15 July the TIMED satellite yawed so that SABER no longer measured the polar summer MLT. Thus, hereafter we analyze results only up to ~15 July, during which both MLS and SABER were each contributing data to the polar summer MLT assimilation. The system generates regularly gridded global analysis fields of geopotential heights, temperatures, water vapor and ozone mixing ratios, horizontal winds, and other quantities every 6 h at 60 reference pressure levels distributed roughly evenly in pressure height over the range 1000–0.0005 hPa.

As the assimilation proceeded, quality checks were performed by comparing zonal-mean temperature output with separate bias-corrected MLS and SABER zonal means computed from 2 days of data. While MLS and SABER each provide good global coverage over 2 days, their local time sampling is limited and different. Figs. 3 and 4 plot examples of such comparisons for 24 June 2007. Differences are plotted in the lower panel of these figures, and are all generally small at altitudes below ~0.01 hPa.

At higher altitudes, Fig. 3 reveals a warm bias relative to bias-corrected MLS at the equator and subtropics that is not seen in the SABER comparison in Fig. 4. The feature is too broad latitudinally and too stationary in time to be explained by aliasing of the diurnal tide, and seems to reflect systematic biases between the two measurements. Additionally, the forecast model does not reproduce a realistic semiannual oscillation of the equatorial MLT with the current GWD settings due to insufficient tropical GW flux, an issue currently being addressed separately by tropical GWD tuning experiments over climate time scales with the forecast model.

In the polar summer MLT, the analysis is slightly colder than bias-corrected MLS in Fig. 3 and slightly warmer than SABER in Fig. 4 (i.e., SABER is colder than bias-corrected MLS). If anything, version 1.07 SABER temperatures may have a warm bias above ~86 km altitude in the polar summer MLT (Kutepov et al., 2006; Remsberg et al., 2008). This suggests our global-mean MLS bias correction may be making initially cold-biased MLS temperatures slightly too warm in the polar summer MLT. Since the intrinsic vertical resolution of MLS temperature retrievals exceeds 10 km at these altitudes, this inferred warm bias may indicate vertical smearing of sharply decreasing polar mesopause temperature structure in MLS retrievals, structure captured better by higher vertical resolution SABER measurements (see also Figs. 2e and f). If so, our use of constant vertical averaging widths for MLS data in the DAS may also be problematic here.

Next we compared assimilated fields with preliminary retrievals from SOFIE. These comparisons serve two purposes. First, as measurements not assimilated into the system, SOFIE data provide independent validation of the analysis. Second, SOFIE retrievals are at an early stage of development (Gordley et al., 2008) and can themselves benefit from validation studies. Thus, these comparisons should be viewed as mutual cross-validation of two independent emerging AIM-related products.

Fig. 5a compares SOFIE temperatures from the northern hemisphere between 66° and 69°N from 25 May to 23 June with analyzed temperature profiles from NOGAPS-ALPHA at the nearest longitude, latitude and time of each SOFIE measurement (433 profiles in all). Fig. 5b plots the corresponding mean bias and standard deviation. SOFIE temperatures are close to the bias-corrected MLS and SABER temperatures assimilated by NOGAPS-ALPHA at most altitudes from 100 to 0.01 hPa. The ~5 K warm bias near the stratopause is a SOFIE retrieval issue, related to blending separate high- and low-altitude retrievals at these interface altitudes (Gordley et al., 2008), and is in the process of being corrected, highlighting the usefulness of NOGAPS-ALPHA analyses as an early validation standard for emerging retrieval products from AIM. The standard deviation increases with height in Fig. 5b may be due to resolved gravity waves in the NOGAPS-ALPHA forecasts.

Fig. 6 plots the corresponding comparisons for χ_{H_2O}, showing a small SOFIE wet bias throughout the stratosphere and a slight dry bias in the mesosphere with respect to the MLS water vapor fields

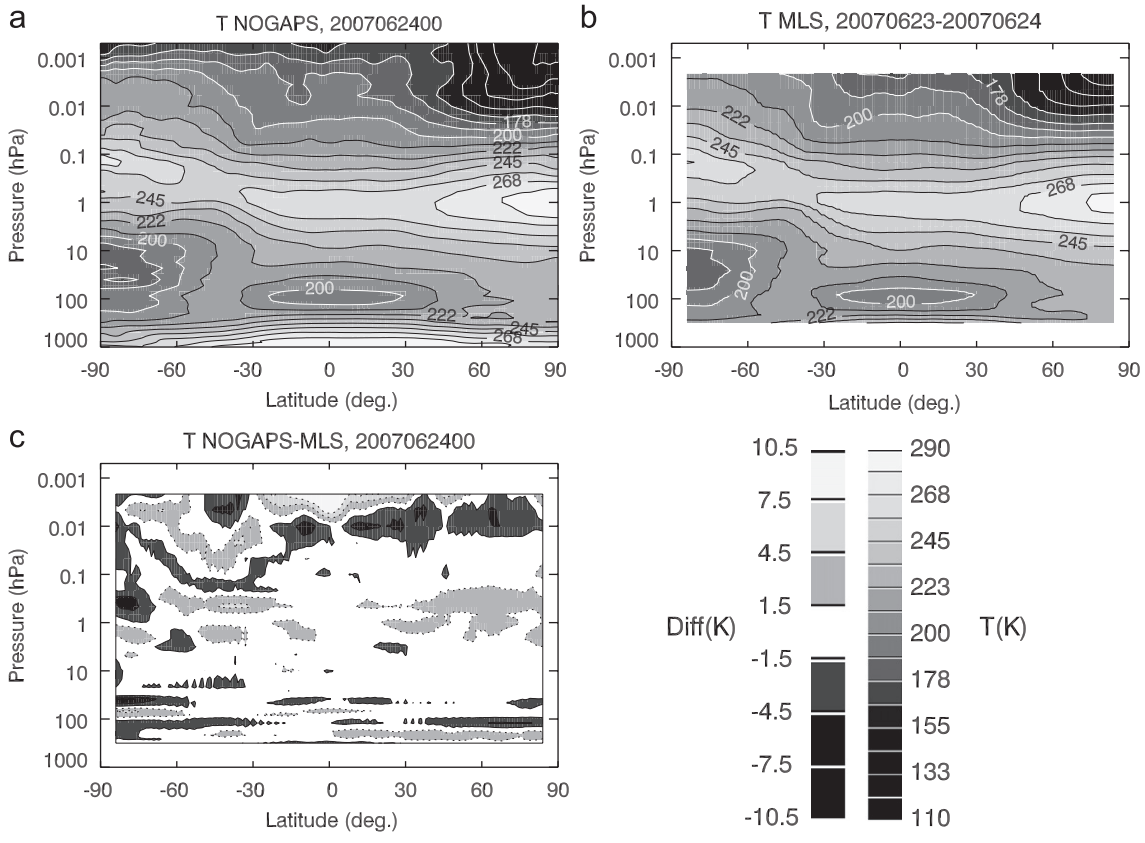

Fig. 3. Zonal-mean temperatures from (a) NOGAPS-ALPHA analysis on 24 June 2007, (b) bias-corrected MLS on 23–24 June 2007, and (c) differences between (a) and (b).

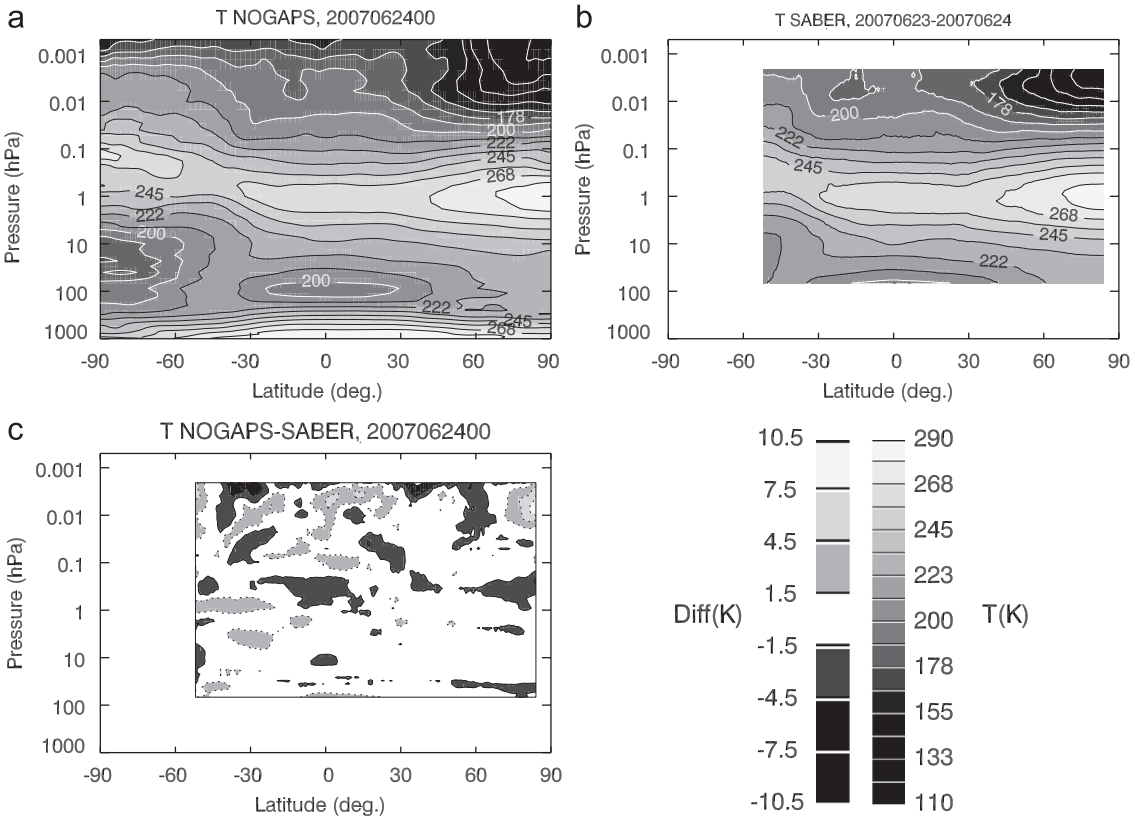

Fig. 4. Same presentation as Fig. 3 but using bias-corrected SABER temperatures.

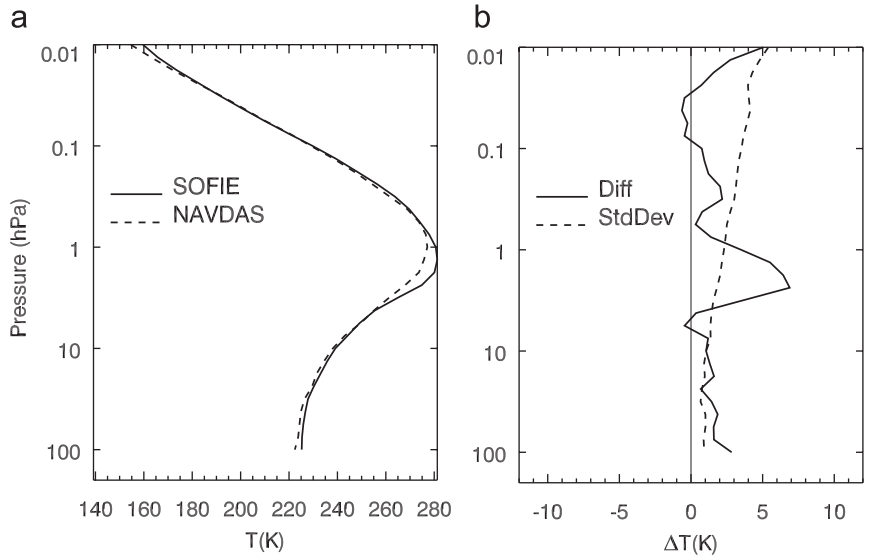

Fig. 5. (a) Mean temperatures from 25 May to 23 June 2007 between 66° and 69°N from 433 retrieved SOFIE profiles (solid) and the NOGAPS-ALPHA analysis at the closest longitude, latitude and time to each SOFIE measurement (dashed); (b) corresponding mean bias (solid) and standard deviation (dashed) between the two.

assimilated by NOGAPS-ALPHA. The mesospheric bias may point to a small wet bias in MLS χ_{H_2O} retrievals (Lambert et al., 2007), since these data have much coarser vertical resolution than SOFIE and thus may underestimate vertical gradients here. Our water vapor analysis shows no evidence of the large dry bias found in some stratospheric humidity analyses due to unrealistic background error covariances (Thornton et al., 2008), indicating that our static background variances and vertical correlation lengths (~2 km) are broadly appropriate.

Finally Fig. 7 compares zonal-mean zonal winds, temperatures and ozone mixing ratios for June 2007 with those from a more mature lower-altitude DAS: the NASA GEOS4 (Bloom et al., 2005). While the GEOS4 runs extend to 0.01 hPa, the standard analysis fields are issued only to 0.2 hPa as shown in Fig. 7b. The overall

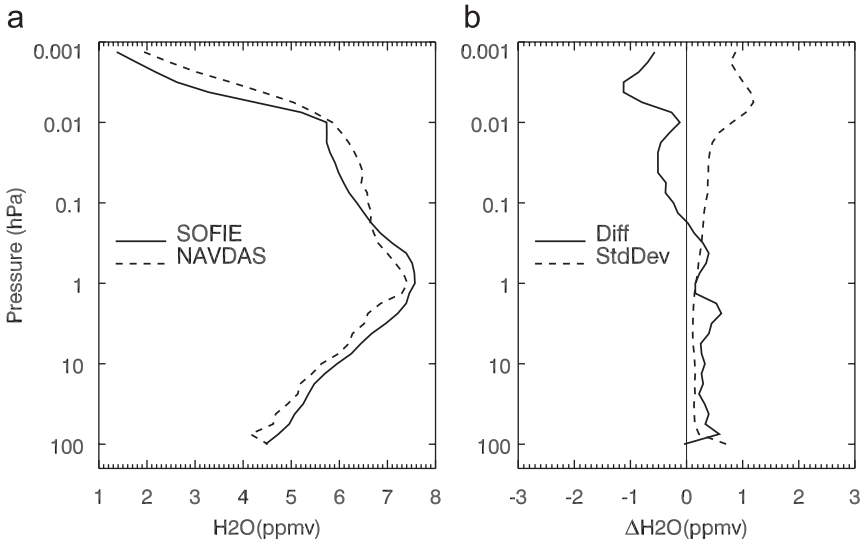

Fig. 6. Same presentation as in Fig. 5 but for χ_{H_2O} (in ppmv).

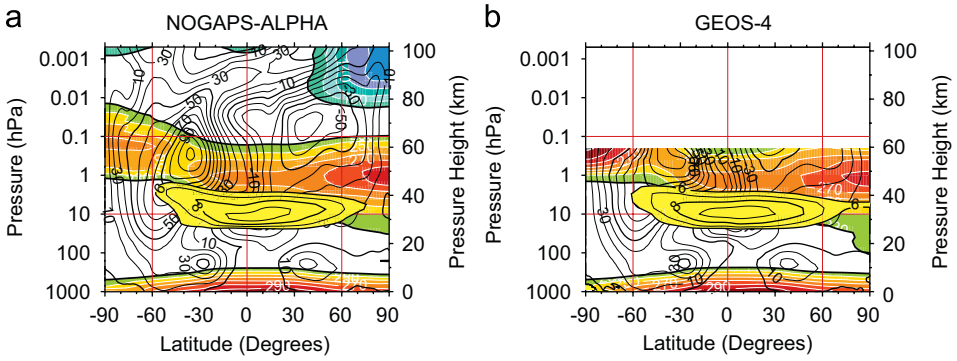

Fig. 7. Comparison of monthly mean zonal-mean analysis output for June 2007 from (a) NOGAPS-ALPHA and (b) NASA GEOS4, showing zonal winds (m s^{-1}, black contours), temperatures (K, rainbow color scale and white contours), and ozone mixing ratios (ppmv, black contours in foreground yellow).

morphology of the mean zonal winds and stratopause temperature structure is very similar in both analyses, apart from temperature differences near the polar winter stratopause. While the GWD parameter settings in NOGAPS-ALPHA may yield forecast biases in the winter hemisphere (see Section 3), the NOGAPS-ALPHA polar winter stratopause temperatures compare better to MLS than the GEOS4 values (note that the TIMED satellite's yaw cycle had SABER preferentially viewing high northern latitudes at this time: see Fig. 4). The zonal-mean peak ozone mixing ratios near 10 hPa are also very similar between the two analyses. The NOGAPS-ALPHA results at higher altitudes in Fig. 7a show closure of the extratropical mesospheric zonal wind jets in both hemispheres and a cold mean polar summer mesopause. We now look in more detail at the polar summer MLT as described by the NOGAPS-ALPHA analysis fields.

5. Mean variations during PMC season

Here we study mean MLT thermal conditions at polar summer latitudes, using analyzed temperature and humidity fields to compute ice supersaturations which we then compare with independent AIM PMC observations. We focus on the results at 0.006 hPa since, during June 2007 at 45°–90°N, this pressure surface lies within the geometric height interval of 83 ± 1 km where bright MCs are typically observed by ground-based instruments (e.g., Lübken et al., 1996). Geometric heights above sea level were computed by rescaling analyzed geopotential heights (e.g., Stull, 2000).

Fig. 8 plots the time variation of temperature at 0.006 hPa averaged between 65° and 70°N. The analysis captures a gradual march to lower temperatures through May and June, yielding cold values in late June and mid July. These plots show spatial variability and temporal intermittency on both large and small scales throughout the season, some of which can immediately be seen to be geophysical. For example, around 5–15 July a wavenumber-1 oscillation with a period of ~5 days is evident in the left panel of Fig. 8. Quasi 5-day waves in temperatures and other analyzed parameters are studied in greater depth in Section 6.

Next we combine NOGAPS-ALPHA temperatures T and water vapor mixing ratios χ_{H_2O} to derive diagnostic saturation ratios for ice,

$$S = \frac{p_{H_2O}}{p_{ice}}, \tag{8}$$

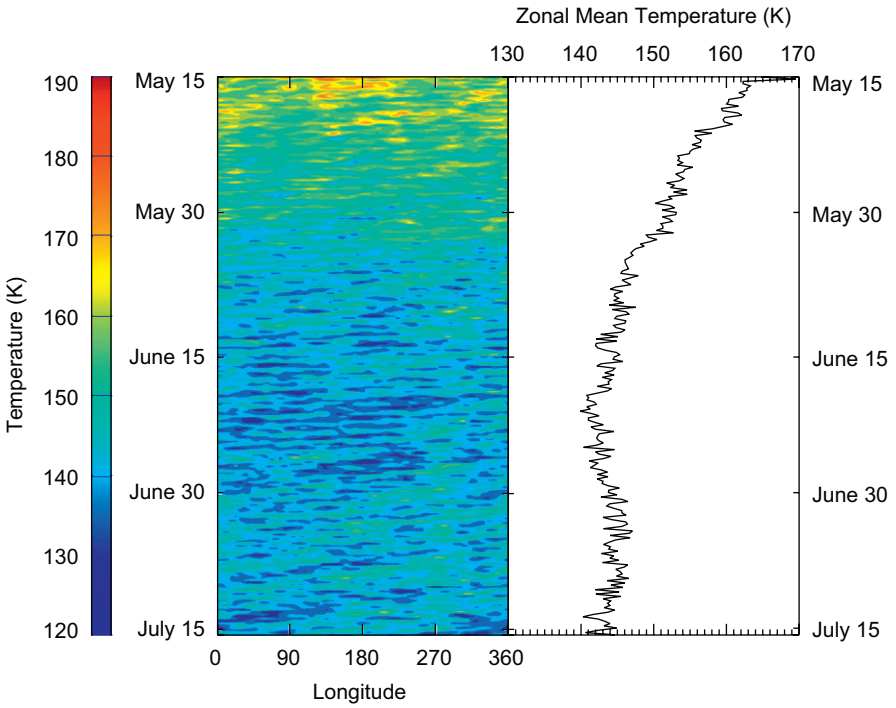

Fig. 8. Plot of mean temperatures between 65° and 70°N at 0.006 hPa from 15 May to 15 July 2007, shown in Hovmöller form on the left and the corresponding zonal-mean temperature time series on the right.

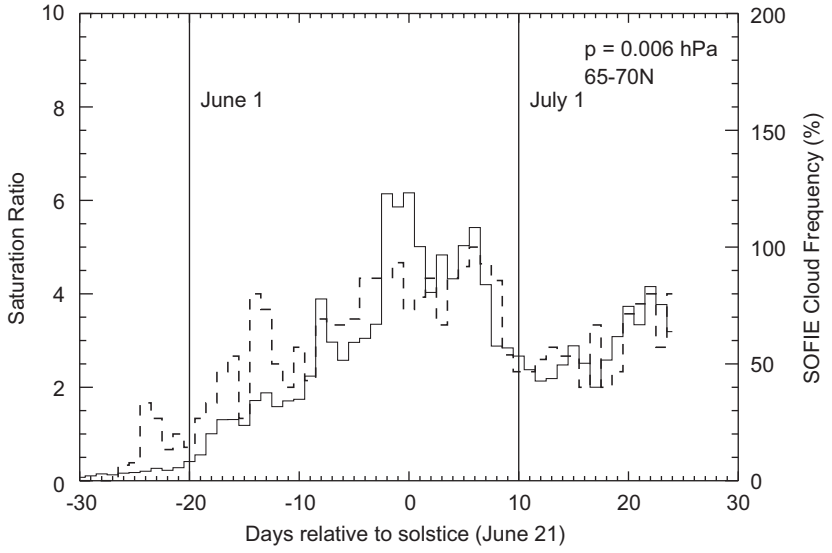

Fig. 9. NOGAPS-ALPHA diurnal-mean saturation ratio S (solid curve, left axis) at 0.006 hPa between 65° and 70°N compared with occurrence frequency of bright PMCs observed by SOFIE (dashed curve, right axis) taken from Fig. 5 of Stevens et al. (2008). The linear correlation coefficient between the two curves is 0.86.

at PMC altitudes, as follows. At a given analysis pressure p, the partial pressure of water vapor $p_{H_2O} = p\chi_{H_2O}$. We specify the saturation vapor pressure for ice, p_{ice}, using the Murphy and Koop (2005) fit

$$\log p_{ice} = 9.550426 - \frac{5723.265}{T} + 3.53068 \log T - 0.00728332T, \quad (9)$$

which is valid for $T \geqslant 110$ K, and thus valid for PMC studies (Rapp and Thomas, 2006).

Fig. 9 plots the time series of zonal-mean diurnally averaged NOGAPS-ALPHA saturation ratios S at 0.006 hPa and 65°–70°N. Ground-based observations report strong correlations between S and PMC occurrence frequency (e.g., Lübken, 1999). Thus we compare our S curve to PMC occurrence frequencies based on SOFIE cloud measurements that were processed by Stevens et al. (2008) to yield sensitivities similar to earlier ground-based and satellite cloud measurements. The resulting curve, taken from Fig. 5 of Stevens et al. (2008) and plotted as the dashed curve in Fig. 9, is highly correlated with S, with an overall linear correlation coefficient of 0.86. Thus these SOFIE PMC data independently validate our temperature and humidity (S) analyses in the polar summer MLT. In typical PMC seasons both curves increase monotonically to maxima in early July, decreasing

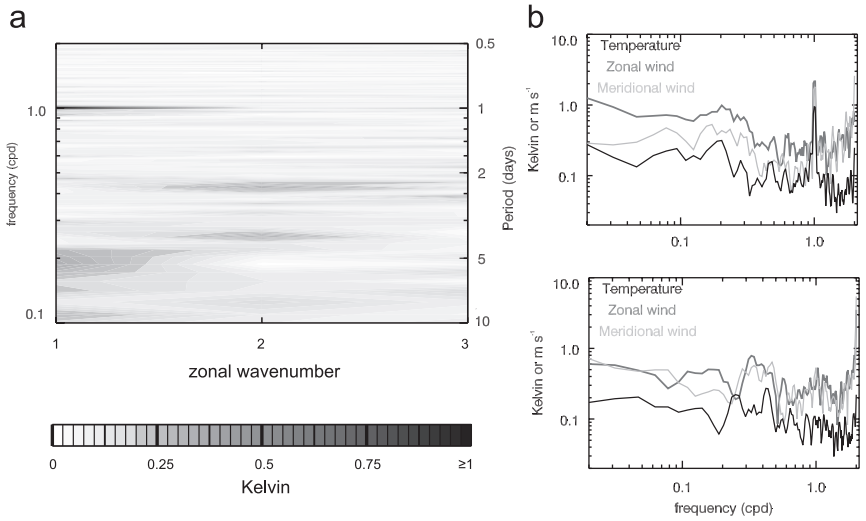

Fig. 10. (a) Wavenumber-frequency amplitude spectrum of temperature at 0.006 hPa and 65°N for westward propagating wavenumbers 1–3 computed over period 15 May to 18 July, 2007. Right panels plot one-dimensional cross sections at (a) wavenumber 1 and (b) wavenumber 2 of temperature and zonal and meridional winds.

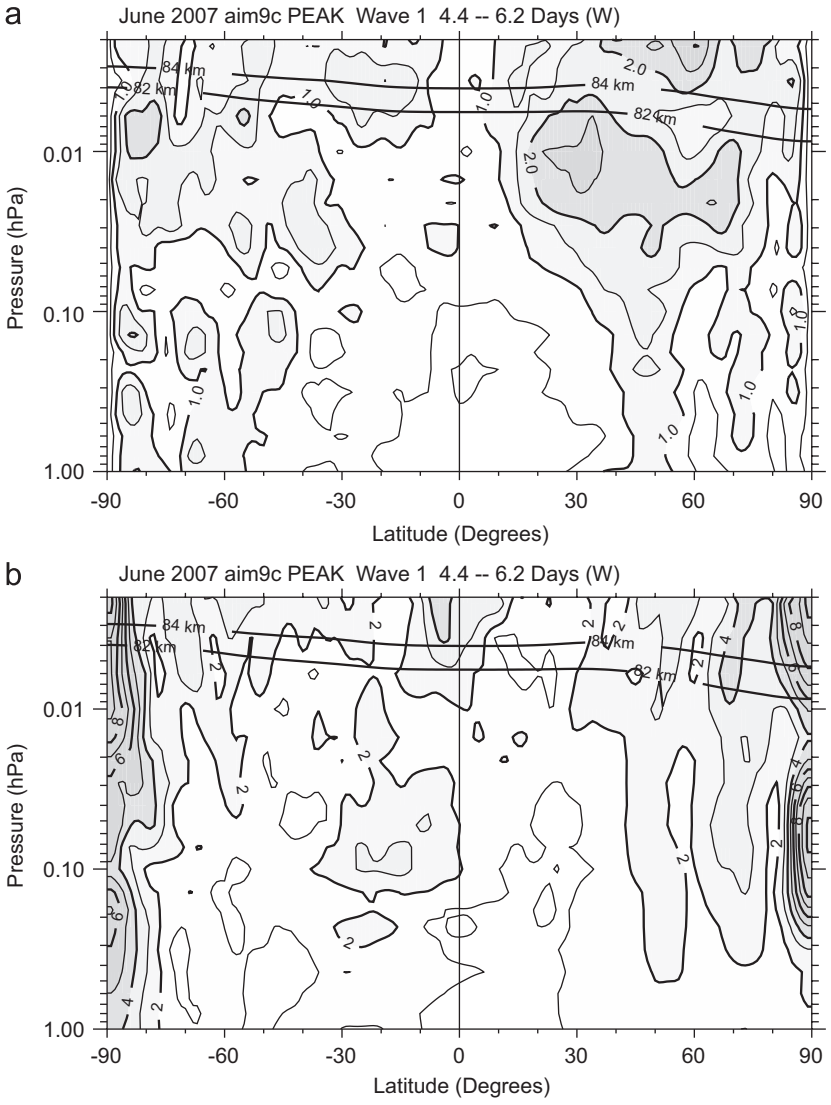

Fig. 11. Peak amplitudes of (a) temperature (K) and (b) meridional wind ($m\,s^{-1}$) of the quasi 5-day wave computed over the 4.4-6.2 day period band at westward wavenumber 1 from NOGAPS-ALPHA analyses for all of June 2007. Black quasi-horizontal contours on each panel show the zonal- and monthly mean 82 km and 84 km geometric height surfaces.

monotonically thereafter (Lübken, 1999). Particularly noteworthy in Fig. 9, therefore, is the sudden decrease in SOFIE PMC frequency in late June and early July followed by a secondary increase thereafter, features also seen in CIPS and Solar Backscatter Ultraviolet (SBUV/2) data (Benze et al., 2008). This distinctly nonclimatological feature is reproduced accurately in the diagnostic NOGAPS-ALPHA S values, and occurs due to ~5 K increases in zonal-mean temperatures at 0.006 hPa at these latitudes at the end of June, followed by a subsequent decrease in temperatures into mid-July, as seen in Fig. 8.

6. Planetary waves

As discussed in the introduction, accurate extraction of tides and fast planetary waves from asynoptic satellite data alone is difficult. Analysis systems like NOGAPS-ALPHA offer a potentially powerful tool for improving data-based planetary wave estimates. Here we demonstrate the capability by performing space-time spectral analysis of the 6-hourly NOGAPS-ALPHA fields (Hayashi, 1982) at a range of altitudes to study specific planetary waves relevant to the polar summer MLT and PMCs.

Fig. 10a plots the mean space-time temperature spectrum of westward-propagating disturbances at 0.006 hPa and 65°N from 15 May 2007 to 18 July 2007. It shows peaks at wavenumber 1 at ~5 days due to the westward-propagating (1,1) Rossby normal mode and at 1 day due to the migrating solar diurnal tide (see Fig. 10b). At wavenumber 2 we also find a migrating semidiurnal tidal signal, most strongly in horizontal winds (see Fig. 10c). We analyze these planetary wave signals in greater depth in what follows. Analysis of the ~2 day wavenumber-2 Rossby normal mode (Merkel et al., 2008a), which also appears in Figs. 10a and c, is left for future studies.

6.1. Quasi 5-day wave

A number of studies have reported modulations in PMC occurrence frequency by the quasi 5-day (1,1) Rossby normal mode (e.g., Kirkwood et al., 2002; Merkel et al., 2003; von Savigny et al., 2007; Merkel et al., 2008a). Fig. 11 shows mean values of peak temperature and meridional wind amplitude in June 2007, derived by scaling by $\sqrt{2}$ the RMS spectral power at westward-propagating wavenumber 1 over the 4.4–6.2 day period band. Inferred temperature amplitudes peak at midlatitudes and are weak at the equator, a latitudinal structure in broad agreement with previous modeling and observations (Hirota and Hirooka, 1984; Riggin et al., 2006). Peak amplitudes are generally weak with monthly mean values in Fig. 11a of ~1−3 K in the summer MLT, in the range of previous observational estimates (e.g., von Savigny et al., 2007). Meridional wind responses, an indirect product of the assimilation, peak in Fig. 11b primarily at the poles.

Fig. 12a plots the time evolution of high-latitude 5-day wave temperature amplitudes at our nominal PMC surface of 0.006 hPa (~83 km altitude: see Fig. 11). These maps result from digitally filtering the spectral components to isolate westward zonal wavenumber 1 within the 4.4–6.25 day period band, inverse transforming back to the space-time domain, then computing oscillation amplitudes around a latitude circle at each latitude and time. The temperature amplitudes in Fig. 12a show considerable time variation, periodically intensifying then disappearing during May and June, and attaining largest amplitudes in early July at midlatitudes. By contrast, Merkel et al. (2008b) reported enhanced 5-day wave amplitudes in SABER temperatures centered near 78°N on 1 July, which drove an associated 5-day-wave enhancement in CIPS PMC albedo. This SABER feature peaked at ~88 km altitude and attenuated rapidly below 85 km (Merkel et al., 2008b), altitudes above the 0.006 hPa surface (~83 km) in Fig. 12a. Thus Fig. 12b plots amplitudes at a higher altitude analysis surface of 0.0013 hPa, which reproduce the 1 July peak near 78°N reported by Merkel et al. (2008b). Fields at 0.0013 hPa lie above the highest data insertion level of 0.002 hPa and so are controlled mostly by the forecasts.

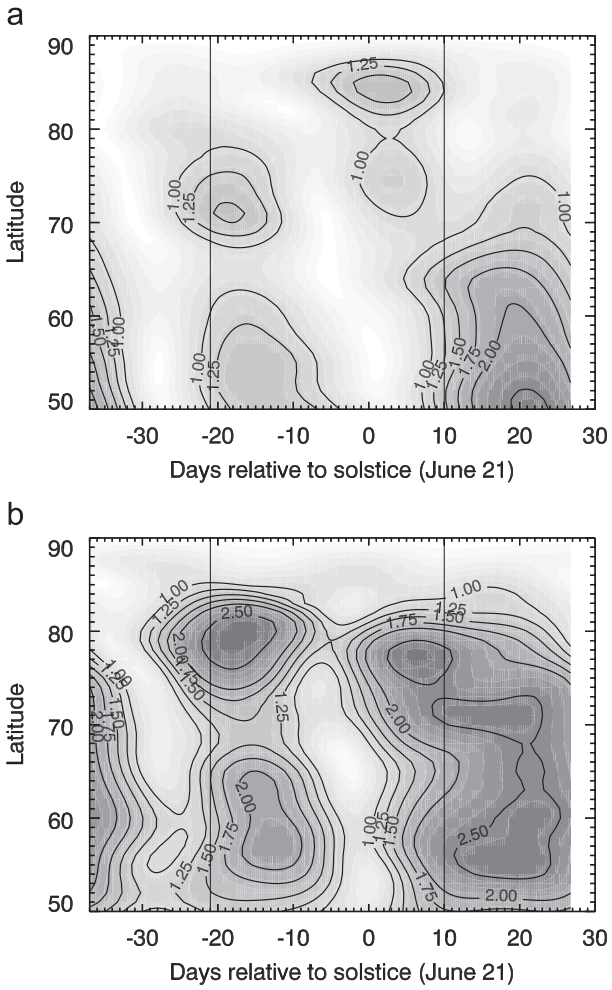

Fig. 12. Time series versus northern latitude of quasi 5-day wave peak amplitude in temperature (K) at (a) 0.006 hPa and (b) 0.0013 hPa. First day of June and July is marked with solid vertical line in each panel.

6.2. Solar migrating tides

Fig. 13 plots peak amplitudes of the migrating diurnal tide averaged over the entire June 2007 analysis period, derived from spectral signals at westward-propagating wave-1 in a narrow frequency band centered at 1 day^{-1}. Fig. 13a reveals an equatorial temperature peak of ~5−10 K maximizing at lower altitudes slightly south of the equator, and a meridional wind peak of ~25 m s^{-1} at ~25°S. Both results are in fairly good agreement with long-term data-validated CMAM results for June (cf. Fig. 2 of McLandress, 2002). Temperature amplitudes also agree well with amplitudes inferred from SABER temperatures during June 2004 by Zhang et al. (2006) and from UARS MLS temperatures by Forbes et al. (2006). At higher altitudes tidal peaks of ~4−8 K also occur at extratropical summer MLT altitudes. One caveat to this latter result is that MLS shows systematically larger day-night

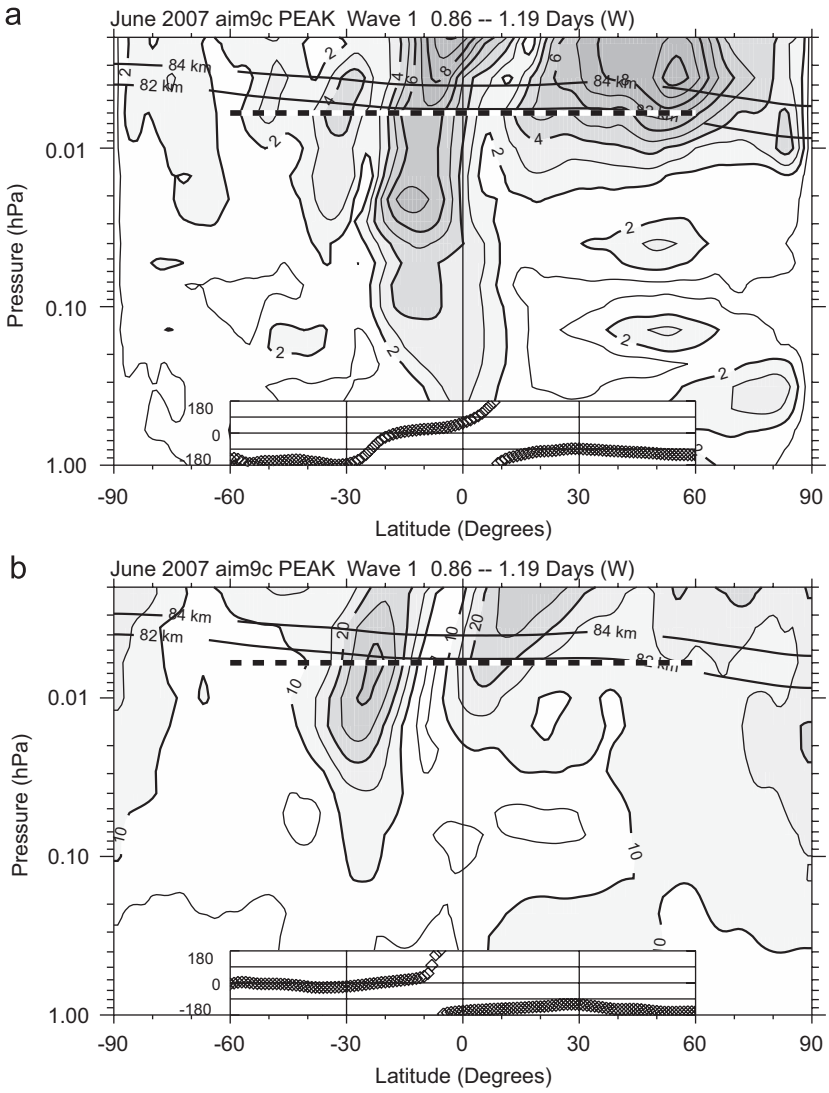

Fig. 13. Peak amplitudes of (a) temperature (K) and (b) meridional wind ($m\,s^{-1}$) of the migrating diurnal tide computed over the 0.86–1.19 day period band. Black quasi-horizontal contours on each panel show the zonal- and monthly mean 82 and 84 km geometric height surfaces. Mean phase variations along the black-and-white dashed line between 60°S and 60°N at 0.006 hPa are plotted in the lower inset panels as the longitude (°E) of local maximum at 0000 UTC.

differences in temperature in the summer MLT than either SABER or the forecasts. These differences remain unexplained at present.

Fig. 14 shows corresponding results for the migrating semidiurnal tide. Accurate assimilation of semidiurnal tides is particularly challenging, since they lie at the Nyquist period of our 6 h analysis window. Moreover, the periodic variation in the 6-hourly longitudinal window for MLS and SABER data insertion essentially migrates with the Sun and may act as an artificial forcing term. Thus these semidiurnal results warrant careful scrutiny.

Peak temperature amplitudes in Fig. 14a show an extended high-altitude temperature peak at ~40°S in broad agreement with tidal models (see Zhang et al., 2006). June 2004 SABER results of Zhang et al. (2006) show a secondary peak nearer the equator: similar peaks are evident in Fig. 14a. In the summer MLT temperature amplitudes are weaker in broad agreement with observations (e.g., Singer et al., 2003).

Our semidiurnal meridional-wind amplitudes in Fig. 14b show two broad extratropical peaks peaking at ±50−60° latitude of up to ~20−30 $m\,s^{-1}$. Long-term radar measurements of winds in the Arctic MLT show smaller climatological peak meridional wind amplitudes of ~10−20 $m\,s^{-1}$ (Portnyagin et al., 2004). However, MLT winds measured by a meteor radar at Kühlungsborn (54°N) suggested stronger semidiurnal wind amplitudes of ~20−30 $m\,s^{-1}$ in June 2007 (Stevens et al., 2008). Thus Fig. 15 compares monthly mean zonal and meridional winds for June 2007 as a function of local time measured by the Kühlungsborn radar (Singer et al., 2003) and corresponding analysis values. Given the coarse 6 h local time resolution, that no MLT wind measurements were assimilated, and that winds are strongly coupled geostrophically to temperature by NAVDAS at these latitudes (Daley and Barker, 2001b) which may be questionable in the summer MLT (McLandress et al., 2006), the analyzed NOGAPS-ALPHA wind fields do surprisingly well in capturing the amplitude and phase of the semidiurnal tidal winds measured by the radar.

6.3. *Planetary wave signals in water vapor*

Fig. 16 shows the quasi 5-day wave and diurnal tidal amplitude responses in NOGAPS-ALPHA assimilated water vapor fields. The 5-day wave amplitudes in Fig. 16a show a vertically broad peak in the summer MLT maximizing at ~60°–75°N. The peak amplitudes are ~0.2−0.3 ppmv in the lower mesosphere. These findings are

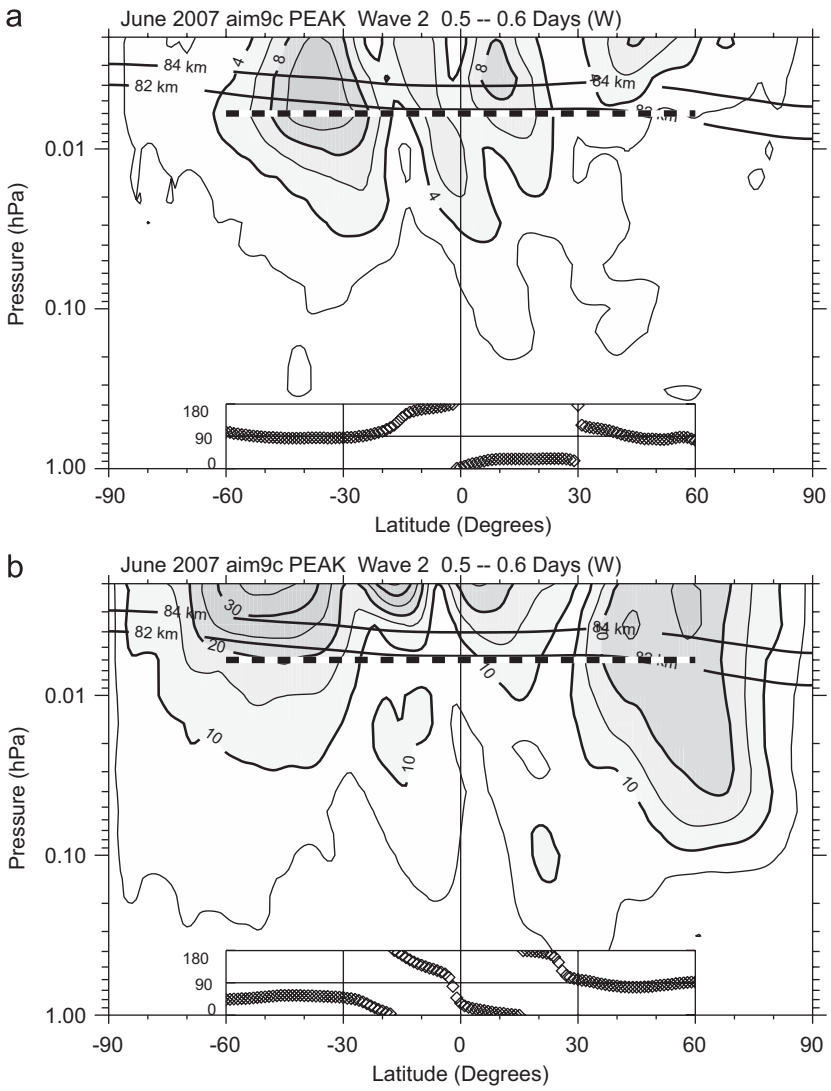

Fig. 14. As for Fig. 13 but showing migrating semidiurnal tidal amplitudes averaged over the 0.5–0.6 day period band.

consistent with ground-based microwave water vapor data from 69°N analyzed by Sonnemann et al. (2008), which show quasi 5-day oscillations of similar magnitude at a range of lower mesospheric altitudes in summer. They used a global model to explain these features in terms of 5-day wave-modulated horizontal transport across mean latitudinal water vapor gradients. In Fig. 16b we also see water vapor signals due to the diurnal tide in the midlatitude lower mesosphere at ~0.1 hPa.

In the upper mesosphere, where strong anticorrelations between the 5-day wave in temperature and PMC brightness are observed (von Savigny et al., 2007; Merkel et al., 2008a), unexplained phase offsets of up to 30° can occur (Merkel et al., 2008a,b). Merkel et al. (2008a) speculated that these latter cases may result from additional 5-day-wave influences on water vapor. To investigate possible correlations with water vapor mixing ratios, Fig. 17 plots spectral cross coherences versus frequency at westward wavenumber 1 using analysis fields at 65°N and 0.006 hPa. While temperature and meridional wind show statistically significant coherence at ~5 days, neither parameter exhibits a statistically significant correlation with water vapor at ~5 days. Since errors in individual MLS χ_{H_2O} estimates are large at these altitudes (Lambert et al., 2007), this lack of coherence may simply reflect an inability to measure small wave-induced water vapor anomalies with sufficient accuracy, particularly since 5-day wave amplitudes in June 2007 are fairly weak (Fig. 11). Furthermore, the coarse MLS vertical resolution may smear out sharp vertical gradients in water driven by PMC formation at high altitudes and sublimation at lower altitudes on quasi-5-day periods, which higher resolution instruments like SOFIE resolve better (e.g., Fig. 12 of Russell et al., 2008). Since water vapor anomalies are photolyzed on time scales of a few days in the polar summer MLT (McCormack et al., 2008), this may also damp water vapor responses to the 5-day wave. Thus, 5-day wave signals in water vapor mixing ratios at PMC altitudes in Fig. 16a may be a complex net result of temperature-modulated PMC deposition and sublimation (Merkel et al., 2008a), photolytic water vapor loss (McCormack et al., 2008) and transport across mean χ_{H_2O} gradients (Sonnemann et al., 2008).

By contrast, statistically significant correlations exist among diurnal tidal responses in temperature, meridional wind and water vapor in Fig. 17. The relative roles of tidal temperatures and winds in controlling PMCs and summer MLT water vapor are currently unclear. Despite fairly large tidal temperature amplitudes (Fig. 13a), tidal signals in χ_{H_2O} correlate more strongly with the tide's meridional wind oscillations. The mean cross spectral phase between the meridional wind and χ_{H_2O} tidal responses is close to −90°. Since meridional tidal displacements are 90° out of phase with meridional wind oscillations, then the peak tidal χ_{H_2O}

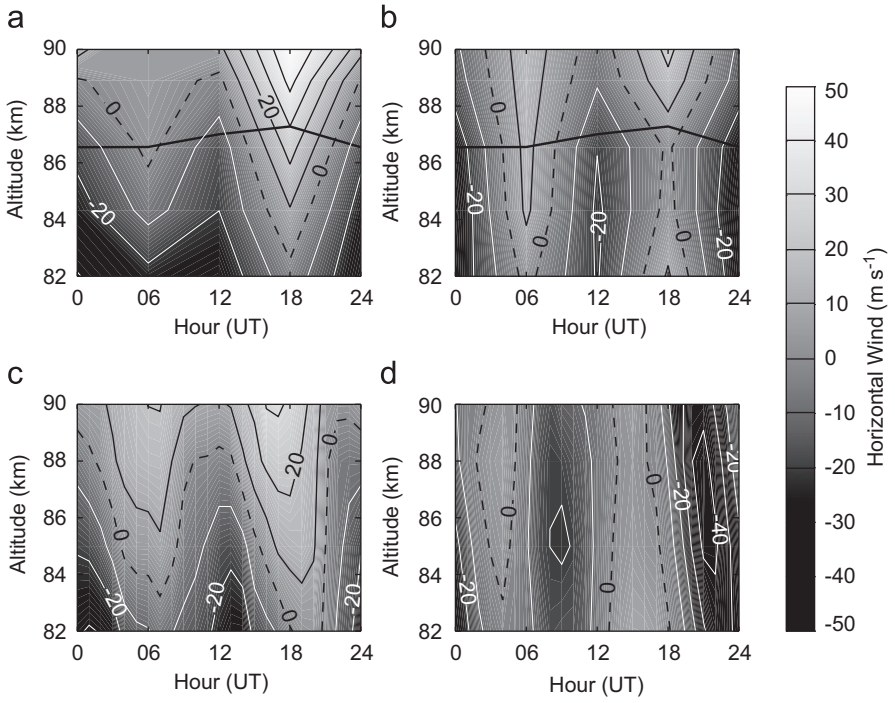

Fig. 15. Monthly mean (a) zonal and (b) meridional winds ($m\,s^{-1}$) as a function of universal time and geometric height for June 2007 over Kühlungsborn (54.1°N, 11.8°E) from NOGAPS-ALPHA analysis. Quasi-horizontal black contour shows mean geometric height of the 0.0022 hPa surface, the approximate level where data insertion abates and results relax to pure model fields above. Lower panels show corresponding (c) zonal and (d) meridional winds measured by the meteor radar at Kühlungsborn (Singer et al., 2003). Eastward and northward (westward and southward) winds are plotted with solid black (white) contours.

perturbations roughly coincide with maximum latitudinal parcel excursions due to the tide, suggesting an important role for tidal transport across meridional gradients in generating these tidal water vapor signals.

7. Sporadic mid-latitude MCs

Equatorward of 50° latitude, MCs are considered by many as a novelty, where they are more popularly referred to as noctilucent clouds (NLCs: Taylor et al., 2002; Thomas et al., 2003; Deland et al., 2006). They are of global importance, however, because the transition region in an environmental system is considered to be the most sensitive to change. Theoretical studies consistently indicate that climate trends should manifest themselves first in midlatitude MCs (Thomas, 1996; Siskind et al., 2005). Yet the MC events that occur episodically at midlatitudes are not well understood (see, e.g., Herron et al., 2007). The global synoptic perspective provided by assimilated MLT temperatures and humidities from NOGAPS-ALPHA should be well suited to the identification and scientific investigation of MC events. Here we explore the potential for identification only, leaving the deeper interpretation of the fundamental thermal, dynamical and microphysical processes that seeded each MC outbreak for subsequent research.

Our approach is as follows. Since supersaturation is a necessary (but insufficient) condition for clouds to form and grow, then, assuming fast time scales for sublimation in unsaturated air, observed MCs should exist either within supersaturated air masses, or in close proximity in time and/or space. If, furthermore, MCs occur over a region large enough to be resolved by NOGAPS-ALPHA, S maps computed from assimilated NOGAPS-ALPHA temperature and humidity fields should reveal supersaturation ($S>1$) when and where MCs are observed, while unsaturated air in the analysis should be devoid of large-scale MCs. In this way, these highly transient and localized MC events provide stringent independent observational tests of the NOGAPS-ALPHA MLT analysis. We consider three separate MC/NLC events observed in June 2007.

7.1. MC event of 13 June 2007

The Spatial Heterodyne Imager for Mesospheric Radicals (SHIMMER) on STPSat-1 (Space Test Program Satellite-1) is a limb-viewing UV imager (Englert et al., 2008). The limb view geometry makes SHIMMER well suited to detecting dimmer PMCs at lower latitudes since, unlike nadir sounders, the cloud signal does not need to be discriminated from a bright background.

Fig. 18a plots all 236 UV limb profiles from 66 to 100 km altitude acquired by SHIMMER on 13 June 2007 between 40° and 50°N. After removing the Rayleigh background using the technique described by Stevens et al. (2008), three profiles on this day, plotted in gray in Fig. 18a, indicate the presence of a MC at ~80 km altitude (Fig. 18b).

The geographical locations of these three profiles are shown with red dots in Fig. 19c. Successive panels in Fig. 19 plot maps of the assimilated NOGAPS-ALPHA temperature, water vapor mixing ratios and saturation ratios S at 0.006 hPa over the North American and Pacific regions on 13 June at 1800 UTC. These synoptic maps show an outbreak of cold mid-latitude MLT air below 150 K over the northern Pacific and northwestern US on this day. These low temperatures extend to nearly 40°N and yield saturation ratios well in excess of unity across isolated regions of the northwestern US and northeastern Pacific where the three cloud events in Fig. 18 were detected.

Identical maps at adjacent times and altitudes were also studied (not shown). At 0.0036 hPa analyzed 1800 UTC temperatures over the northwestern US drop below 130 K, yielding local supersaturations >100, whereas at 0.01 hPa there is no supersaturation equatorward of 60°N. At 0.006 hPa, there is essentially no supersaturation equatorward of 60°N and 50°N at 0000 UTC

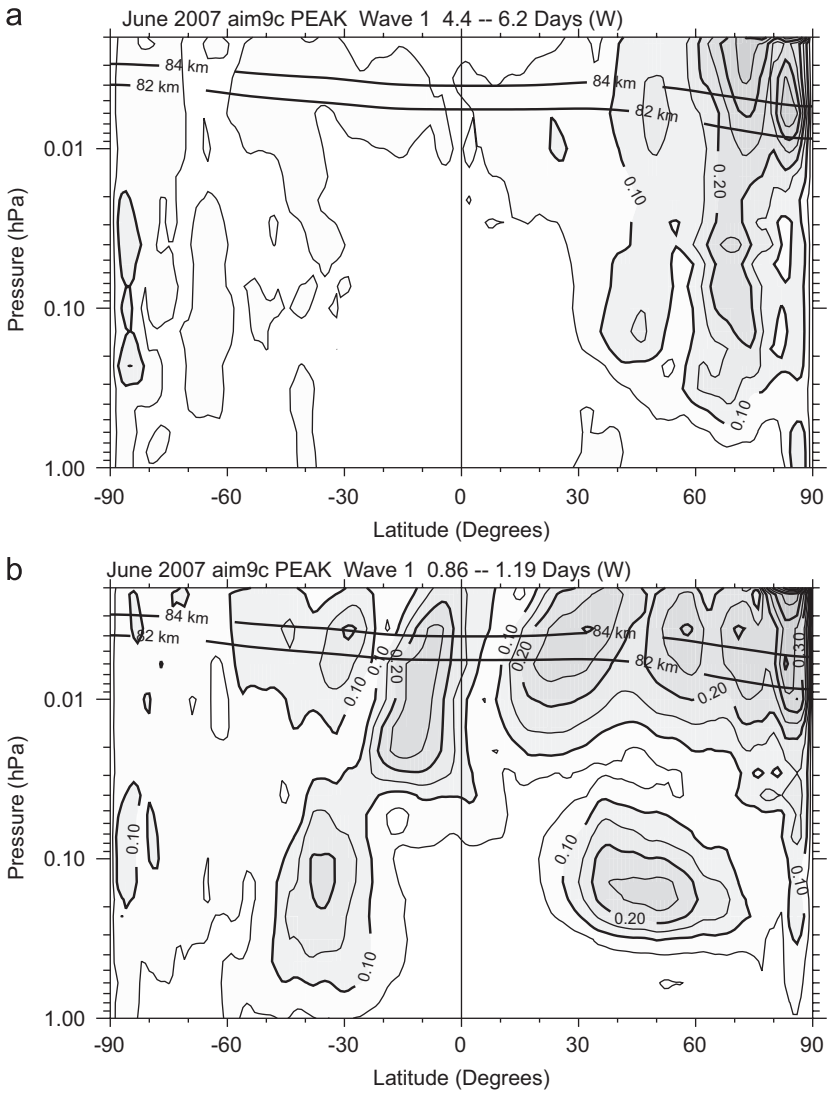

Fig. 16. Peak χ_{H_2O} amplitudes (ppmv) for the (a) quasi 5-day wave and (b) migrating diurnal tide for June 2007. Black quasi-horizontal contours on each panel show the zonal- and monthly mean 82 and 84 km geometric height surfaces.

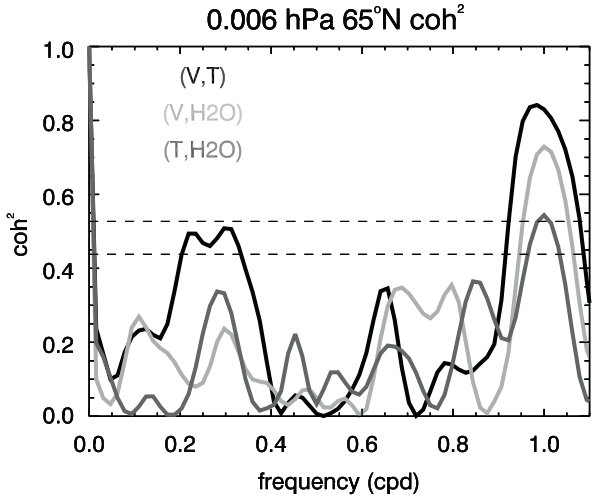

Fig. 17. Cross coherence spectra versus frequency at westward wavenumber 1 among temperature, meridional wind and water vapor analysis fields at 65°N and 0.006 hPa, based on time series from 15 May to 18 July. Dotted lines show 90% and 95% confidence levels, following Thompson (1979).

and 0600 UTC, respectively. At 1200 UTC isolated areas of moderate supersaturation have formed over the northwestern US and off the west coast over the Pacific. After peaking at 1800 UTC (Fig. 19c), 6 h later this supersaturated midlatitude air has disappeared, leaving essentially no supersaturated air equatorward of 60°N. These findings are consistent with the highly transient and geographically isolated nature of these observed clouds.

These comparisons show that the diagnostic estimate of saturation ratio *S* based on analyzed NOGAPS-ALPHA temperature and water vapor fields shows skill in identifying this mid-latitude burst of MCs observed by SHIMMER. The maps indicate that mid-latitude MCs can exist here at this time due to the cold supersaturated local environment, without the need in this case for additional local subgrid-scale cooling from gravity wave temperature perturbations (e.g., Rapp et al., 2002).

7.2. NLC event of 19–20 June 2007

In the late evening hours of 19 June 2007 and into the morning of 20 June, spectacular displays of NLCs were widely reported and

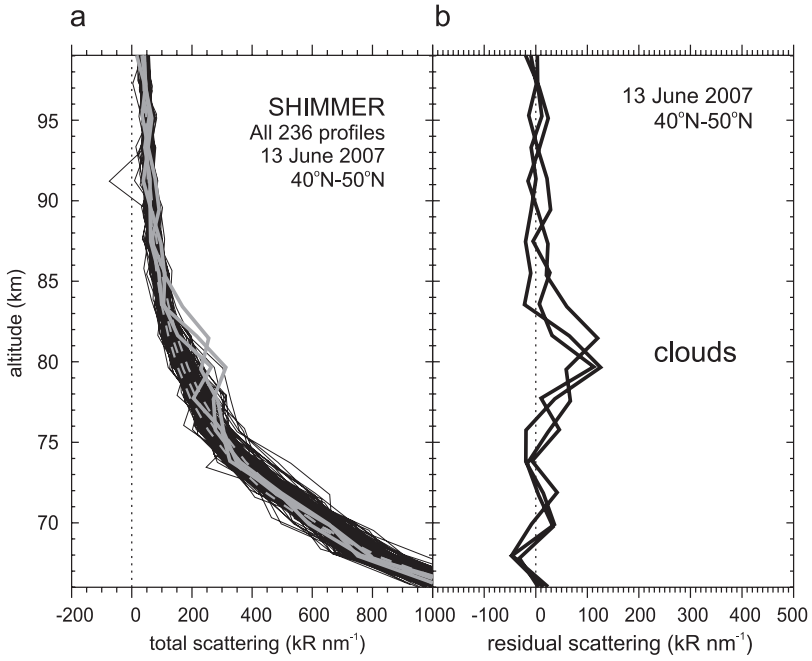

Fig. 18. (a) All 236 limb brightness profiles acquired by SHIMMER between 40° and 50°N on 13 June 2007. Profiles are dominated by Rayleigh scattering. Three of these profiles (solid gray curves) show a statistically significant enhancement from the fitted Rayleigh background (dotted gray curves), which is subtracted in (b) to show the residual signal due to mesospheric cloud scattering at ~80 km. The locations of these three measurements are shown in Fig. 19c and occurred (going from west to east) at 1649 UTC, 1650 UTC and 1513 UTC.

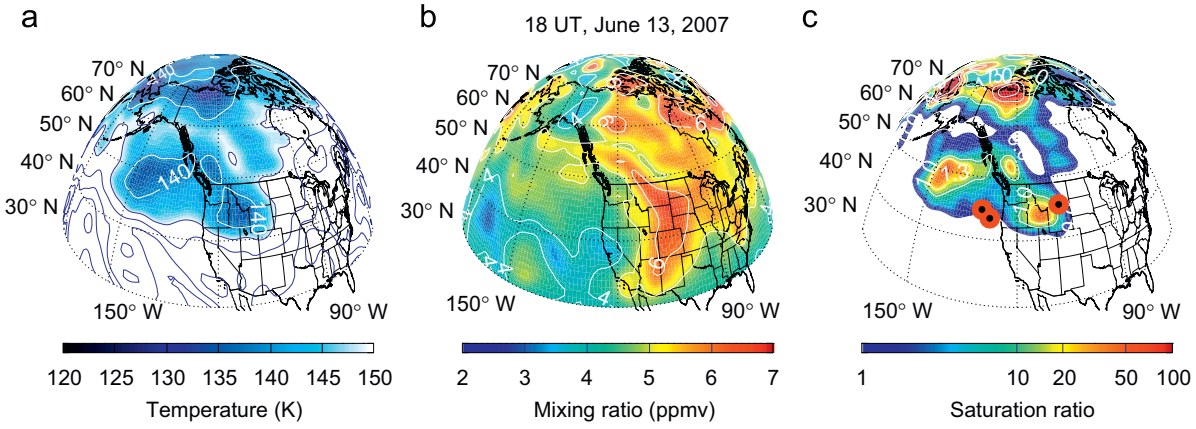

Fig. 19. Maps of analyzed NOGAPS-ALPHA (a) temperature (K), (b) water vapor mixing ratio (ppmv), and (c) saturation ratio S at 0.006 hPa on 13 June 2007 at 1800 UTC. Filled red circles with black interior dots in panel c show the locations of the three MCs detected by SHIMMER in Fig. 18b.

photographed by many amateur observers in Washington state and Oregon in the western United States[1], with bright NLCs photographed as far south as Bend, Oregon (44.0°N). The ground-based NLC observing network of Dalin et al. (2008) also reported bright NLCs on this date at its Canadian station.

Fig. 20 plots the same sequence of 0.006 hPa temperature, water vapor and saturation ratios from the NOGAPS-ALPHA analysis of 20 June at 0600 UTC. The mesosphere over the northwestern US region is again cold, characterized by a tongue of cold air in Fig. 20a that extends equatorward from polar regions and within which moderate supersaturations occur in Fig. 20c. Results at 1800 UTC (not shown) show this same feature has migrated westward to lie over the Pacific in a similar band of latitudes. The diagnostic S values from NOGAPS-ALPHA therefore appear consistent with these observed mid-latitude NLCs.

7.3. NLC event of 30 June 2007

NLCs were reported and photographed[2] on 29–30 June 2007 from many regions in Europe, including Sweden, Denmark, the United Kingdom, France, Germany, Hungary, and even as far south as Palmela, Portugal at 38.6°N. Dalin et al. (2008) reported bright NLCs on this night from stations in Scotland, Sweden, Denmark and Russia.

[1] see, e.g., http://www.spaceweather.com/nlcs/gallery2007_page4.htm

[2] see http://www.spaceweather.com/nlcs/gallery2007_page6.htm; http://www.kersland.plus.com/nlc2007.htm.

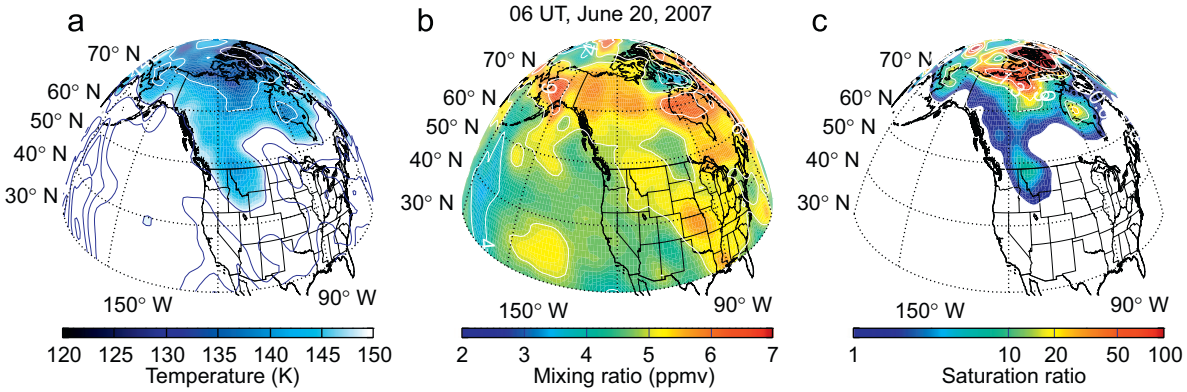

Fig. 20. Same presentation as Fig. 19 but showing NOGAPS-ALPHA fields at 0.006 hPa on 20 June 2007 at 0600 UTC.

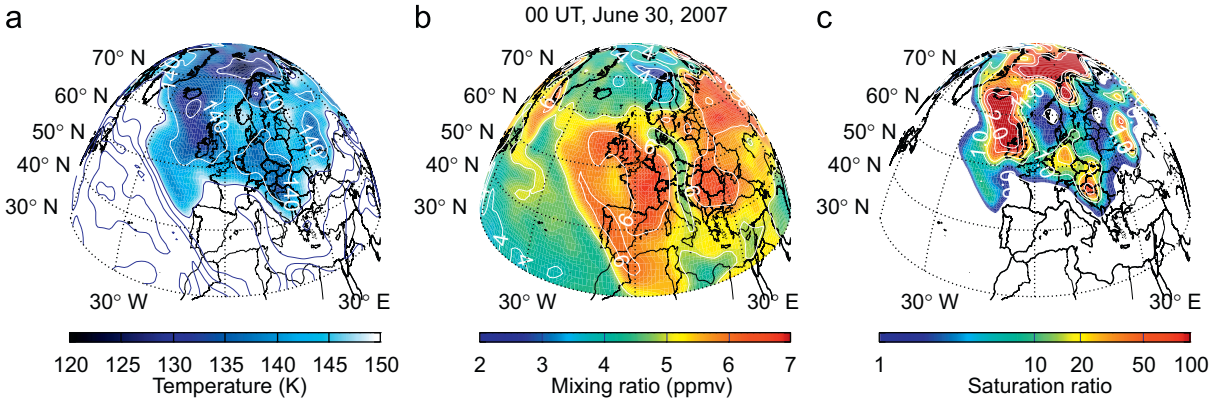

Fig. 21. Same presentation as Fig. 19 but showing NOGAPS-ALPHA fields at 0.006 hPa on 30 June 2007 at 0000 UTC centered over western Europe.

The NOGAPS-ALPHA 0.006 hPa analysis fields on 30 June 2007 at 0000 UTC in Fig. 21 show an extensive pool of cold mesospheric air over northwestern Europe. Particularly interesting in this event are broad regions of enhanced water vapor mixing ratios in Fig. 21b over the United Kingdom, France, Spain, the Balkans and Russia. These water vapor enhancements combine with low temperatures to yield large supersaturations in Fig. 21c over, for example, the United Kingdom and Hungary where bright NLCs were observed. Again, the widespread reports of NLC displays over Europe at this time are borne out by enhanced mid-latitude saturation ratios in Fig. 21c over broad swaths of the continent, further validating our analyzed NOGAPS-ALPHA MLT temperature and water vapor fields.

8. Summary and outlook

We have presented first results of a specific high-altitude assimilation of MLS and SABER temperatures and MLS water vapor and ozone mixing ratios using a new version of NOGAPS-ALPHA containing a full DAS component that extends from the ground to MLT altitudes. These experiments were carefully designed, tuned and performed during the northern summer MLT season of 2007, the first PMC season measured by instruments on AIM. We focused on analysis fields between mid-May and mid-July when both MLS and SABER were observing the polar summer MLT.

We validated our assimilation against independent measurements. Assimilated temperatures showed small biases with respect to SABER, MLS, SOFIE and GEOS4 at most altitudes and latitudes. Analyzed horizontal winds, derived indirectly from assimilated temperatures and model forecasts, compared favorably with GEOS4 in the stratosphere and with meteor radar measurements in the MLT. Combining assimilated water vapor and temperature fields into saturation ratios S yielded excellent agreement with seasonal variations in SOFIE measurements of PMC occurrence frequency. These diagnostic S fields also reproduced the occurrence times and geographic locations of several separate mid-latitude MC/NLC events observed by SHIMMER and ground-based observers during June 2007.

Spectral signatures of the quasi 5-day (1,1) Rossby normal mode and solar migrating diurnal and semidiurnal tides were isolated from the analyses and investigated as a function of height, latitude, and time. The 5-day wave temperature amplitudes at PMC altitudes of $\sim 1-3$ K were similar to those inferred in previous studies. A clear 5-day wave signal in water vapor mixing ratios in the polar summer MLT was also revealed, but did not correlate linearly with the 5-day wave in temperature or meridional wind. Latitude-height distributions of diurnal and semidiurnal tidal amplitudes appeared to be broadly realistic, despite the intrinsic limitations of the 6-hourly 3DVAR data insertion process. For example, the amplitude and phase of semidiurnal tidal winds were quite similar to those measured by a meteor radar. The diurnal tide produced a water vapor signal in the polar summer MLT that correlated with meridional tidal winds in ways that suggest major contribution from latitudinal tidal advection, although there is a smaller but still significant correlation with tidal temperatures too.

These preliminary results underscore how emerging ground-to-MLT global analysis fields provided by this and other NWP

systems (e.g., Polavarapu et al., 2005a) offer new opportunities for MLT science. Within the specific context of AIM and PMCs, these fields can be used to investigate systematically some of the major scientific issues, such as: hemispheric asymmetries in summer polar MLT temperatures and PMC amount (Siskind et al., 2003; Lübken and Berger, 2007); planetary wave modulation of PMCs (von Savigny et al., 2007); relative roles of vertical and horizontal transport on mid-latitude PMCs (Gerding et al., 2007), and; possible global teleconnections between PMCs in one hemisphere and polar stratospheric meteorological conditions in the other hemisphere (Karlsson et al., 2007). In helping to answer these and other specific questions, these MLT fields can begin to address deeper questions about the fundamental character of the MLT itself. For example, how predictable is the MLT (Hoppel et al., 2008)? Is MLT transport mainly local or nonlocal, and more specifically, is long-range horizontal transport in the MLT predictable or fundamentally chaotic (e.g., Holton and Schoeberl, 1988; Shepherd et al., 2000; Stevens et al., 2003)?

That having been said, current ground-to-MLT forecast-assimilation systems, including this one, are at the very early stages of their development and there is much left to do to improve them for future studies. In addition to assimilation of new data (e.g., SSMIS), new and improved model parameterizations and DAS algorithms are needed to handle the MLT region better (e.g., Polavarapu et al., 2005b; Sankey et al., 2007). Among the near-term foci for NOGAPS-ALPHA development are more completely tuned nonorographic GWD parameterizations for all latitudes and seasons, more complete diabatic heating and cooling rate parameterizations for the MLT, parameterizations of ozone chemistry in the MLT, NNMI algorithms that work well in the MLT, better MLT bias correction schemes, and higher-altitude radiative forward models $\mathscr{H}$ for direct assimilation of MLT radiances into the system (Han et al., 2007). As the AIM mission continues through 2008 and beyond, it will continue to offer a superb testbed environment for developing and validating these capabilities, which in turn should hopefully feed back to add value to AIM measurements and enhance the science return of this mission.

Acknowledgments

This research was supported by NASA, the Office of Naval Research, the Defense Threat Reduction Agency, and a grant of computer time from the DoD High Performance Computing Modernization Program at the Naval Oceanographic Office (NAVO) and Air Force Research Laboratory (AFRL) Major Shared Resource Centers. SHIMMER is a joint project between NRL and the DoD Space Test Program. We thank Victor Fomichev for his generous assistance with his radiative heating and cooling rate codes, and two anonymous reviewers for helpful comments.

References

Alexander, M.J., Dunkerton, T.J., 1999. A spectral parameterization of mean flow forcing due to breaking gravity waves. Journal of the Atmospheric Sciences 56, 4167–4182.

Allen, D.R., Coy, L., Eckermann, S.D., McCormack, J.P., Manney, G.L., Hogan, T.F., Kim, Y.-J., 2006. NOGAPS-ALPHA simulations of the 2002 Southern Hemisphere stratospheric major warming. Monthly Weather Review 134, 498–518.

Arakawa, A., Suarez, M.J., 1983. Vertical differencing of the primitive equations in sigma coordinates. Monthly Weather Review 111, 34–45.

Azeem, S.M.I., Killeen, T.L., Johnson, R.M., Wu, Q., Gell, D.A., 2000. Space-time analysis of TIMED Doppler Interferometer (TIDI) measurements. Geophysical Research Letters 27, 3297–3300.

Baker, N.L., Hogan, T.F., Campbell, W.F., Pauley, R.L., Swadley, S.D., 2005. The impact of AMSU-A radiance assimilation in the U.S. Navy's Operational Global Atmospheric Prediction System (NOGAPS). Naval Research Laboratory Memorandum Report, NRL/MR/7530-05-8836, 22pp.

Baker, N.L., Goerss, J., Sashegyi, K., Pauley, P., Langland, R., Xu, L., Blankenship, C., Campbell, B., Ruston, B., Rosmond, T., Pauley, R.L., 2007. An overview of the NRL Atmospheric Variational Data Assimilation (NAVDAS) and NAVDAS-AR (Accelerated Representer) Systems. In: 18th AMS Conference on Numerical Weather Prediction, 25–29 June, Park City, UT, Paper 2B.1, 6pp. Available at: ⟨http://ams.confex.com/ams/pdfpapers/124031.pdf⟩.

Ballish, B., Cao, X., Kalnay, E., Kanamitsu, M., 1992. Incremental nonlinear normal-mode initialization. Monthly Weather Review 120, 1723–1734.

Becker, E., Fritts, D.C., 2006. Enhanced gravity-wave activity and interhemispheric coupling during the MaCWAVE/MIDAS northern summer program 2002. Annales Geophysicae 24, 1175–1188.

Benze, S., Randall, C.E., DeLand, M.T., Thomas, G.E., Rusch, D.W., Bailey, S.M., Russell III, J.M., McClintock, W., Merkel, A.W., Jeppesen, C., 2008. Comparison of polar mesospheric cloud measurements from the cloud imaging particle size experiment and the solar backscatter ultraviolet instrument in 2007. Journal of Atmospheric and Solar-Terrestrial Physics, this issue.

Berger, U., von Zahn, U., 2007. Three-dimensional modeling of the trajectories of visible noctilucent cloud particles: an indication of particle nucleation well below the mesopause. Journal of Geophysical Research 112, D16204.

Bloom, S., da Silva, A., Dee, D., Bosilovich, M., Chern, J.-D., Pawson, S., Schubert, S., Sienkiewicz, M., Stajner, I., Tan, W.-W., Wu, M.-L., 2005. In: Suarez, M.J. (Ed.), Documentation and Validation of the Goddard Earth Observing System (GEOS) Data Assimilation System—Version 4. NASA Technical Memorandum NASA/TM-2005-104606. Technical Report Series on Global Modeling and Data Assimilation, vol. 15, 165pp. Available online at: ⟨http://ntrs.nasa.gov⟩.

Burrage, M.D., Hagan, M.E., Skinner, W.R., Wu, D.L., Hays, P.B., 1995. Long-term variability in the solar diurnal tide observed by HRDI and simulated by the GSWM. Geophysical Research Letters 22, 2641–2644.

Charron, M., Manzini, E., 2002. Gravity waves from fronts: parameterization and middle atmosphere response in a general circulation model. Journal of the Atmospheric Sciences 59, 923–941.

Chou, M.-D., Suarez, M.J., 1999. In: Suarez, M.J. (Ed.), A Solar Radiation Parameterization for Atmospheric Studies. NASA Technical Memorandum NASA/TM-1999-104606. Technical Report Series on Global Modeling and Data Assimilation, vol. 15, 40pp. Available at: ⟨http://ntrs.nasa.gov⟩.

Chou, M.-D., Suarez, M.J., Liang, X.-Z. Liang, Yan M.M.-H., 2001. In: Suarez, M.J. (Ed.), A Thermal Infrared Radiation Parameterization for Atmospheric Studies. NASA Technical Memorandum NASA/TM-2001-104606. Technical Report Series on Global Modeling and Data Assimilation, vol. 19, 56pp. Available at: ⟨http://ntrs.nasa.gov⟩.

Coy, L., Allen, D.R., Eckermann, S.D., McCormack, J.P., Stajner, I., Hogan, T.F., 2007. Effects of model chemistry and data biases on stratospheric ozone assimilation. Atmospheric Chemistry and Physics 7, 2917–2935.

Daley, R., Barker, E., 2001a. NAVDAS: formulation and diagnostics. Monthly Weather Review 129, 869–883.

Daley, R., Barker, E., 2001b. NAVDAS Source Book 2001. Naval Research Laboratory Publication NRL/PU/7530–01-441, 163pp.

Dalin, P., et al., 2008. Ground-based observations of noctilucent clouds with a northern hemisphere network of automatic digital cameras. Journal of Atmospheric and Solar-Terrestrial Physics 70, 1460–1472.

Dee, D., daSilva, A.M., 1998. Data assimilation in the presence of forecast bias. Quarterly Journal of the Royal Meteorological Society 124, 269–295.

DeLand, M.T., Shettle, E.P., Thomas, G.E., Olivero, J.J., 2006. A quarter-century of satellite PMC observations. Journal of Atmospheric and Solar-Terrestrial Physics 68, 9–29.

Drob, D.P., Picone, J.M., Eckermann, S.D., She, C.Y., Kafkalidis, J.F., Ortland, D.A., Niciejewski, R.J., Killeen, T.L., 2000. Mid-latitude temperatures at 87 km: results from multi-instrument Fourier analysis. Geophysical Research Letters 27, 2109–2112.

Eckermann, S.D., 2008. Hybrid $\sigma-p$ coordinate choices for a global model. Monthly Weather Review, in press, doi:10.1175/2008MWR2537.1.

Eckermann, S.D., McCormack, J.P., Coy, L., Allen, D., Hogan, T., Kim, Y.-J., 2004. NOGAPS-ALPHA: a prototype high altitude global NWP model. In: Preprint Volume of the Symposium on the 50th Anniversary of Operational Numerical Weather Prediction, June 2004. American Meteorological Society, University of Maryland, College Park, MD, Paper P2.6, 23pp. Available online at: ⟨http://uap-www.nrl.navy.mil/dynamics/papers/EckermannP2.6-reprint.pdf⟩.

Eckermann, S.D., Broutman, D., Stollberg, M.T., Ma, J., McCormack, J.P., Hogan, T.F., 2007. Atmospheric effects of the total solar eclipse of 4 December 2002 simulated with a high-altitude global model. Journal of Geophysical Research 112, D14105.

Englert, C.R., Stevens, M.H., Siskind, D.E., Harlander, J.M., Roesler, F.L., von Savigny, C., Kochenash, A., 2008. First results from the Spatial Heterodyne Imager for Mesospheric Radicals (SHIMMER): the diurnal variation of mesospheric hydroxyl. Geophysical Research Letters 35, L19813, doi:10.1029/2008GL035420.

Fomichev, V.I., Blanchet, J.-P., Turner, D.S., 1998. Matrix parameterization of the 15 μm CO_2 band cooling in the middle and upper atmosphere for variable CO_2 concentration. Journal of Geophysical Research 103, 11505–11528.

Fomichev, V.I., Ogibalov, V.P., Beagley, S.R., 2004. Solar heating by the near-IR CO_2 bands in the mesosphere. Geophysical Research Letters 31, L21102.

Forbes, J.M., Kilpatrick, M., Fritts, D., Manson, A.H., Vincent, R.A., 1997. Zonal mean and tidal dynamics from space: an empirical examination of aliasing and sampling issues. Annales Geophysicae 15, 1158–1164.

Forbes, J.M., Wu, D., Zhang, X., 2006. Solar tides as revealed by measurements of mesosphere temperature by the MLS experiment on UARS. Journal of the Atmospheric Sciences 63, 1776–1797.
Fritts, D.C., Luo, Z., 1995. Dynamical and radiative forcing of the summer mesopause and thermal structure, 1, mean solstice conditions. Journal of Geophysical Research 100, 3119–3128.
Garcia, R.R., Marsh, D.R., Kinnison, D.E., Boville, B.A., Sassi, F., 2007. Simulation of secular trends in the middle atmosphere, 1950–2003. Journal of Geophysical Research 112, D09301.
Garcia-Comas, M., Lopez-Puertas, M., Marshall, B.T., Wintersteiner, P.P., Funke, B., Bermejo-Pantaleon, D., Mertens, C.J., Remsberg, E.E., Gordley, L.L., Mlynczak, M.G., Russell III, J.M., 2008. Errors in SABER kinetic temperature caused by non-LTE model parameters. Journal of Geophysical Research, in press, doi:10.1029/2008JD010105.
Geer, A.J., Lahoz, W.A., Jackson, D.R., Cariolle, D., McCormack, J.P., 2007. Evaluation of linear ozone photochemistry parametrizations in a stratosphere-troposphere data assimilation system. Atmospheric Chemistry and Physics 7, 939–959.
Gerding, M., Höffner, J., Rauthe, M., Singer, W., Zecha, M., Lübken, F.-J., 2007. Simultaneous observation of noctilucent clouds, mesospheric summer echoes, and temperature at a midlatitude station (54°N). Journal of Geophysical Research 112, D12111.
Gordley, L.L., et al., 2008. The solar occultation for ice experiment. Journal of Atmospheric and Solar-Terrestrial Physics, this issue.
Hamilton, K., 1997. The role of parameterized drag in a troposphere-stratosphere-mesosphere general circulation model. In: Hamilton, K. (Ed.), Gravity Wave Processes—Their Parameterization in Global Climate Models, vol. I 50. Springer, Berlin, Heidelberg, pp. 337–350 NATO ASI Series.
Han, Y., Weng, F., Liu, Q., van Delst, P., 2007. A fast radiative transfer model for SSMIS upper atmosphere sounding channels. Journal of Geophysical Research 112, D11121.
Harshvardhan, Davies, R., Randall, D., Corsetti, T., 1987. A fast radiation parameterization for atmospheric circulation models. Journal of Geophysical Research 92, 1009–1016.
Hayashi, Y., 1982. Space-time spectral analysis and its applications to atmospheric waves. Journal of the Meteorological Society of Japan 60, 156–171.
Herron, J.P., Wickwar, V.B., Espy, P.J., Meriwether, J.W., 2007. Observations of a noctilucent cloud above Logan, Utah (41.7°N, 118.8°W) in 1995. Journal of Geophysical Research 112, D19203.
Hirota, I., Hirooka, T., 1984. Normal mode Rossby waves observed in the upper stratosphere, part 1: first symmetric modes of zonal wavenumbers 1 and 2. Journal of the Atmospheric Sciences 41, 1253–1267.
Hogan, T.F., 2007. Land surface modeling in the Navy Operational Global Atmospheric Prediction System, Paper 11B.1. In: Preprint Volume of 22nd AMS Conference on Weather Analysis and Forecasting/18th Conference on Numerical Weather Prediction, Park City, UT. Available online at: ⟨http://ams.confex.com/ams/22WAF18NWP/techprogram/paper_123403.htm⟩.
Hogan, T.F., Rosmond, T.E., 1991. The description of the navy operational global atmospheric prediction system's spectral forecast model. Monthly Weather Review 119, 1786–1815.
Hogan, T.F., Rosmond, T.E., Gelaro, R., 1991. The NOGAPS forecast model: a technical description. Naval Oceanographic and Atmospheric Research Laboratory Report No. 13, 219pp.
Holton, J.R., Schoeberl, M.R., 1988. The role of gravity wave generated advection and diffusion in transport of tracers in the mesosphere. Journal of Geophysical Research 93, 11075–11082.
Hoppel, K.W., Baker, N.L., Coy, L., Eckermann, S.D., McCormack, J.P., Nedoluha, G., Siskind, D.E., 2008. Assimilation of stratospheric and mesospheric temperatures from MLS and SABER into a global NWP model. Atmospheric Chemistry and Physics 8, 6103–6116.
Jiang, Y.B., et al., 2007. Validation of aura microwave limb sounder ozone by ozonesonde and lidar measurements. Journal of Geophysical Research 112, D24S34.
Karlsson, B., Körnich, H., Gumbel, J., 2007. Evidence for interhemispheric stratosphere-mesosphere coupling derived from noctilucent cloud properties. Geophysical Research Letters 34, L16806.
Kerola, D.X., 2006. Calibration of special sensor microwave imager/sounder (SSMIS) upper air brightness temperature measurements using a comprehensive radiative transfer model. Radio Science 41, RS4001.
Kirkwood, S., et al., 2002. Noctilucent clouds, PMSE, and 5-day planetary waves: a case study. Geophysical Research Letters 29 (10), 1411.
Kutepov, A.A., Feofilov, A.G., Marshall, B.T., Gordley, L.L., Pesnell, W.D., Goldberg, R.A., Russell III, J.M., 2006. SABER temperature observations in the summer polar mesosphere and lower thermosphere: importance of accounting for the CO_2 v_2 quanta V–V exchange. Geophysical Research Letters 33, L21809.
Lahoz, W.A., O'Neill, A., 1998. Atmospheric data assimilation and its role in SPARC. SPARC Newletter 11, 11–16. Available online at: ⟨http://www.aero.jussieu.fr/~sparc/News11/DataAssimilation.html⟩.
Lambert, A., et al., 2007. Validation of the aura microwave limb sounder middle atmosphere water vapor and nitrous oxide measurements. Journal of Geophysical Research 112, D24S36.
Lindzen, R.S., 1981. Turbulence and stress due to gravity wave and tidal breakdown. Journal of Geophysical Research 86, 9701–9714.
Lipton, A.E., 2002. Polarization of measurement for microwave temperature sounding of the mesosphere. IEEE Transactions on Geoscience and Remote Sensing 40, 1669–1681.
Lorenc, A.C., Rawlins, F., 2005. Why does 4D-Var beat 3D-Var? Quarterly Journal of the Royal Meteorological Society 131, 3247–3257.
Louis, J.F., 1979. A parametric model of vertical eddy fluxes in the atmosphere. Boundary Layer Meteorology 17, 187–202.
Louis, J.F., Tiedtke, M., Geleyn, J.F., 1982. A short history of the operational PBL parameterization at ECMWF. In: ECMWF Workshop on Planetary Boundary Parameterizations, 25–27 November 1981, pp. 59–79.
Lübken, F.-J., 1999. Thermal structure of the Arctic summer mesosphere. Journal of Geophysical Research 104, 9135–9149.
Lubken, F.-J., Berger, U., 2007. Interhemispheric comparison of mesospheric ice layers from the LIMA model. Journal of Atmospheric and Solar-Terrestrial Physics 69, 2292–2308.
Lübken, F.-J., Fricke, K.-H., Langer, M., 1996. Noctilucent clouds and the thermal structure near the Arctic mesopause in summer. Journal of Geophysical Research 101, 9489–9508.
Manney, G.L., et al., 2007. Solar occultation satellite data and derived meteorological products: sampling issues and comparisons with aura microwave limb sounder. Journal of Geophysical Research 112, D24S50.
Marsh, D.R., Skinner, W.R., Marshall, A.R., Hays, P.B., Ortland, D.A., Yee, J.-H., 2002. High Resolution Doppler Imager observations of ozone in the mesosphere and lower thermosphere. Journal of Geophysical Research 107 (D19), 4390.
McClintock, W.E., et al., 2008. The cloud imaging and particle size (CIPS) experiment on the aeronomy of ice in the mesosphere (AIM) spacecraft. Journal of Atmospheric and Solar Terrestrial Physics, this issue.
McCormack, J.P., Eckermann, S.D., Coy, L., Allen, D.R., Kim, Y.-J., Hogan, T., Lawrence, B.N., Stephens, A., Browell, E.V., Burris, J., McGee, T., Trepte, C.R., 2004. NOGAPS-ALPHA model simulations of stratospheric ozone during the SOLVE2 campaign. Atmospheric Chemistry and Physics 4, 2401–2423.
McCormack, J.P., Eckermann, S.D., Siskind, D.E., McGee, T.J., 2006. CHEM2D-OPP: a new linearized gas-phase ozone photochemistry parameterization for high-altitude NWP and climate models. Atmospheric Chemistry and Physics 6, 4943–4972.
McCormack, J.P., Hoppel, K.W., Siskind, D.E., 2008. Parameterization of middle atmospheric water vapor photochemistry for high-altitude NWP and data assimilation. Atmospheric Chemistry and Physics Discussions 8, 13999–14032.
McLandress, C., 1998. On the importance of gravity waves in the middle atmosphere and their parameterization in general circulation models. Journal of Atmospheric and Solar-Terrestrial Physics 60, 1357–1383.
McLandress, C., 2002. The seasonal variation of the propagating diurnal tide in the mesosphere and lower thermosphere. Part I: the role of gravity waves and planetary waves. Journal of the Atmospheric Sciences 59, 893–906.
McLandress, C., Zhang, S.P., 2007. Satellite observations of mean winds and tides in the lower thermosphere: 1. Aliasing and sampling issues. Journal of Geophysical Research 112, D21104.
McLandress, C., Ward, W.E., Fomichev, V.I., Semeniuk, K., Beagley, S.R., McFarlane, N.A., Shepherd, T.G., 2006. Large-scale dynamics of the mesosphere and lower thermosphere: an analysis using the extended Canadian middle atmosphere model. Journal of Geophysical Research 111, D17111.
Merkel, A.W., Thomas, G.E., Palo, S.E., Bailey, S.M., 2003. Observations of the 5-day planetary wave in PMC measurements from the Student Nitric Oxide Explorer satellite. Geophysical Research Letters 30 (4), doi:10.1029/2002GL016524.
Merkel, A.W., Garcia, R.R., Bailey, S.M., Russell III, J.M., 2008a. Observational studies of planetary waves in PMCs and mesospheric temperature measured by SNOE and SABER. Journal of Geophysical Research 113, D14202.
Merkel, A.W., Rusch, D.W., Palo, S.E., Russell III, J.M., Bailey, S.M., 2008b. Mesospheric planetary wave activity inferred from AIM-CIPS and TIMED-SABER for the northern summer 2007 PMC season. Journal of Atmospheric and Solar-Terrestrial Physics, this issue.
Mertens, C.J., et al., 2004. SABER observations of mesospheric temperatures and comparisons with falling sphere measurements taken during the 2002 summer MaCWAVE campaign. Geophysical Research Letters 31, L03105.
Murphy, D.M., Koop, T., 2005. Review of the vapour pressures of ice and supercooled water for atmospheric applications. Quarterly Journal of the Royal Meteorological Society 131, 1539–1565.
Norton, W.A., Thuburn, J., 1999. Sensitivity of mesospheric mean flow, planetary waves, and tides to strength of gravity wave drag. Journal of Geophysical Research 104 (D24), 30897–30912.
Oberheide, J., Hagan, M.E., Roble R.G., 2003. Tidal signatures and aliasing in temperature data from slowly precessing satellites. Journal of Geophysical Research 108(A2), 1055, doi:10.1029/2002JA009585 (correction, 2003. Journal of Geophysical Research 108(A5), 1213, doi:10.1029/2003JA009967).
Palmer, T.N., Shutts, G.J., Swinbank, R., 1986. Allevation of a systematic westerly bias in general circulation and numerical weather prediction models through an orographic gravity wave drag parameterization. Quarterly Journal of the Royal Meteorological Society 112, 1001–1039.
Peng, M.S., Ridout, J.A., Hogan, T.F., 2004. Recent modifications of the Emanuel convective scheme in the navy operational global atmospheric prediction system. Monthly Weather Review 132, 1254–1268.
Polavarapu, S., Ren, S., Rochon, Y., Sankey, D., Ek, N., Koshyk, J., Tarasick, D., 2005a. Data assimilation with the Canadian middle atmosphere model. Atmosphere-Ocean 43, 77–100.
Polavarapu, S., Shepherd, T.S., Rochon, Y., Ren, S., 2005b. Some challenges of middle atmosphere data assimilation. Quarterly Journal of the Royal Meteorological Society 131, 3513–3527.

Portnyagin, Y.I., et al., 2004. Monthly mean climatology of the prevailing winds and tides in the Arctic mesosphere/lower thermosphere. Annales Geophysicae 22, 3395–3410.

Rapp, M., Thomas, G.E., 2006. Modeling the microphysics of mesospheric ice particles: assessment of current capabilities and basic sensitivities. Journal of Atmospheric and Solar-Terrestrial Physics 68, 715–744.

Rapp, M., Lübken, F.-J., Müllemann, A., Thomas, G.E., Jensen, E.J., 2002. Small-scale temperature variations in the vicinity of NLC: experimental and model results. Journal of Geophysical Research 107 (D19), 4392.

Read, W.G., et al., 2007. Aura Microwave Limb Sounder upper tropospheric and lower stratospheric H_2O and relative humidity with respect to ice validation. Journal of Geophysical Research 112, D24S35.

Remsberg, E.E., Marshall, B.T., Marshall, Garcia-Comas, M., Krueger, D.A., Lingenfelser, G.S., Martin-Torres, F.J., Mlynczak, M.G., Russell III, J.M., Smith, A.K., Zhao, Y., Brown, C.W., Gordley, L.L., Lopez-Gonzalez, M., Lopez-Puertas, M., She, C.-Y., Taylor, M.J., Thompson, R.E., 2008. Assessment of the quality of the Version 1.07 temperature-versus-pressure profiles of the middle atmosphere from TIMED/SABER. Journal of Geophysical Research 113, D17101.

Riggin, D.M., et al., 2006. Observations of the 5-day wave in the mesosphere and lower thermosphere. Journal of Atmospheric and Solar-Terrestrial Physics 68, 323–339.

Russell III, J.M., et al., 2008. The aeronomy of ice in the mesosphere (AIM) mission: overview and early science results. Journal of Atmospheric and Solar-Terrestrial Physics, this issue.

Sankey, D., Ren, S., Polavarapu, S., Rochon, Y.J., Nezlin, Y., Beagley, S., 2007. Impact of data assimilation filtering methods on the mesosphere. Journal of Geophysical Research 112, D24104.

Sassi, F., Boville, B.A., Kinnison, D., Garcia, R.R., 2005. The effects of interactive ozone chemistry on simulations of the middle atmosphere. Geophysical Research Letters 32, L07811.

Schwartz, M.J., et al., 2008. Validation of the aura microwave limb sounder temperature and geopotential height measurements. Journal of Geophysical Research 113, D15S11.

Seaman, R.S., Bourke, W.P., Steinle, P., Hart, T., Embery, G., Naughton, M., Rikus, L., 1995. Evolution of the Bureau of Meteorology's global assimilation and prediction system. Part 1: analysis and initialization. Australian Meteorological Magazine 44, 1–18.

Shaw, T.A., Shepherd, T.G., 2007. Angular momentum conservation and gravity wave drag parameterization: implications for climate models. Journal of the Atmospheric Sciences 64, 190–203.

Shepherd, T.G., Koshyk, J.N., Ngan, K., 2000. On the nature of large-scale mixing in the stratosphere and mesosphere. Journal of Geophysical Research 105, 12433–12446.

Simmons, A.J., Burridge, D.M., 1981. An energy and angular momentum conserving vertical finite-difference scheme and hybrid vertical coordinates. Monthly Weather Review 109, 758–766.

Singer, W., Bremer, J., Hocking, W.K., Weiss, J., Latteck, R., Zecha, M., 2003. Temperature and wind tides around the summer mesopause at middle and Arctic latitudes. Advances in Space Research 31 (9), 2055–2060.

Siskind, D.E., Eckermann, S.D., McCormack, J.P., Alexander, M.J., Bacmeister, J.T., 2003. Hemispheric differences in the temperature of the summertime stratosphere and mesosphere. Journal of Geophysical Research 108 (D2), 4051.

Siskind, D.E., Stevens, M.H., Englert, C.R., 2005. A model study of global variability in mesospheric cloudiness. Journal of Atmospheric and Solar-Terrestrial Physics 67, 501–513.

Siskind, D.E., Eckermann, S.D., Coy, L., McCormack, J.P., Randall, C.E., 2007. On recent interannual variability of the Arctic winter mesosphere: implications for tracer descent. Geophysical Research Letters 34, L09806.

Slingo, J.M., 1987. The development and verification of a cloud prediction scheme in the ECMWF model. Quarterly Journal of the Royal Meteorological Society 113, 899–927.

Sonnemann, G.R., Hartogh, P., Grygalashvyly, M., Li, S., Berger, U., 2008. The quasi 5-day signal in the mesospheric water vapor concentration at high latitudes in 2003—a comparison between observations at ALOMAR and calculations. Journal of Geophysical Research 113, D04101.

Stevens, M.H., Gumbel, J., Englert, C.R., Grossmann, K.U., Rapp, M., Hartogh, P., 2003. Polar mesospheric clouds formed from space shuttle exhaust. Geophysical Research Letters 30 (10), 1546.

Stevens, M.H., Englert, C.R., Hervig, M., Petelina, S.V., Singer, W., Nielsen, K., 2008. The diurnal variation of noctilucent cloud frequency near 55°N observed by SHIMMER. Journal of Atmospheric and Solar-Terrestrial Physics, this issue.

Stull, R.B., 2000. Meteorology for Scientists and Engineers, second ed. Brooks/Cole, Pacific Grove, CA, 502pp.

Susskind, J., Barnet, C., Blaisdell, J., Iredell, L., Keita, F., Kouvaris, L., Molnar, G., Chahine, M., 2006. Accuracy of geophysical parameters derived from atmospheric infrared sounder/advanced microwave sounding unit as a function of fractional cloud cover. Journal of Geophysical Research 111, D09S17.

Swinbank, R., Orris, R.L., Wu, D.L., 1999. Stratospheric tides and data assimilation. Journal of Geophysical Research 104, 16929–16942.

Taylor, M.J., Gadsden, M., Lowe, R.P., Zalcik, M.S., Brausch, J., 2002. Mesospheric cloud observations at unusually low latitudes. Journal of Atmospheric and Solar-Terrestrial Physics 64, 991–999.

Teixeira, J., Hogan, T., 2002. Boundary layer clouds in a global atmospheric model: simple cloud cover parameterization. Journal of Climate 15, 1261–1276.

Thomas, G.E., 1996. Is the polar mesosphere the miners canary of global change? Advances in Space Research 18, 149–158.

Thomas, G.E., et al., 2003. Comment on ''Are noctilucent clouds truly a ''Miners Canary'' for global change''. Eos 84 (36), 352–353.

Thompson, R.O.R.Y., 1979. Coherence significance levels. Journal of the Atmospheric Sciences 36, 2020–2021.

Thornton, H.E., Jackson, D.R., Bekki, S., Bormann, N., Errera, Q., Geer, A.J., Lahoz, W.A., Rharmili, S., 2008. The ASSET intercomparison of stratosphere and lower mesosphere humidity analyses. Atmospheric Chemistry and Physics Discussions 8, 13507–13553.

Tiedtke, M., 1984. The sensitivity of the time-scale flow to cumulus convection in the ECMWF model. In: Workshop on Large-Scale Numerical Models, 28 November–1 December 1983, ECMWF, pp. 297–316.

Trenberth, K.E., Stepaniak, D.P., 2002. A pathological problem with NCEP reanalyses in the stratosphere. Journal of Climate 15, 690–695.

von Savigny, C., Robert, C., Bovensmann, H., Burrows, J.P., Schwartz, 2007. Satellite observations of the quasi 5-day wave in noctilucent clouds and mesopause temperatures. Geophysical Research Letters 34, L24808.

Webster, S., Brown, A.R., Cameron, D.R., Jones, C.P., 2003. Improvements to the representation of orography in the Met Office Unified Model. Quarterly Journal of the Royal Meteorological Society 129, 1989–2010.

Wergen, W., 1989. Normal mode initialization and atmospheric tides. Quarterly Journal of the Royal Meteorological Society 115, 535–545.

Wu, D.L., Hays, P.B., Skinner, W.R., 1995. A least squares method for spectral analysis of space-time series. Journal of the Atmospheric Sciences 52, 3501–3511.

Zhang, X., Forbes, J.M., Hagan, M.E., Russell III, J.M., Palo, S.E., Mertens, C.J., Mlynczak, M.G., 2006. Monthly tidal temperatures 20–120 km from TIMED/SABER. Journal of Geophysical Research 111, A10S08.

Zhu, X., Yee, Yee, J.-H., Talaat, E.R., Mlynczak, M., Gordley, L., Mertens, C., Russell III, J.M., 2005. An algorithm for extracting zonal mean and migrating tidal fields in the middle atmosphere from satellite measurements: applications to TIMED/SABER-measured temperature and tidal modeling. Journal of Geophysical Research 110, D02105.